

See discussions, stats, and author profiles for this publication at: <https://www.researchgate.net/publication/270162698>

Long Reach RSOA based Passive Optical Networks

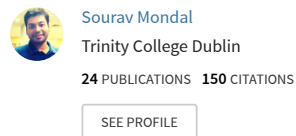
Book · October 2014

DOI: 10.13140/2.1.2029.9843

CITATIONS
0

READS
587

1 author:



Some of the authors of this publication are also working on these related projects:

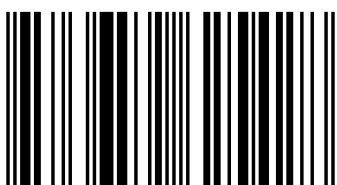
Project Long Reach RSOA based Passive Optical Networks [View project](#)

Project Cyber-Foraging with Cloudlets for Low-Latency Applications [View project](#)

The present access services like video on demand, live streaming, online gaming etc. require enormous amount of bandwidth and traditional digital subscriber line technology fails to meet up this requirement. The next generation networks, in particular, hybrid WDM-TDM Long-Reach Passive Optical Networks provide the required bandwidth and reduce the operational expenditure. Laser sources used at the Optical Network Units increase the cost due the extra equipment required for stabilizing the operating wavelength. To overcome this, a centralized source is installed at the Optical Line Terminal and the signal is reflected and intensity-modulated at the ONU, by using a special optical device Reflective Semiconductor Amplifier (RSOA), thus making the end receiver unit "colourless". The analytical model for RSOA has been described in detailed in this book. The primary objective of this enitre work is to examine the feasibility of hybrid WDM-TDM LR-PON physical layer uplink setup consisting of reflective ONUs with due consideration to the BER performance in presence of realistic and non-ideal characteristics of optical and optoelectronic devices used in the setup.



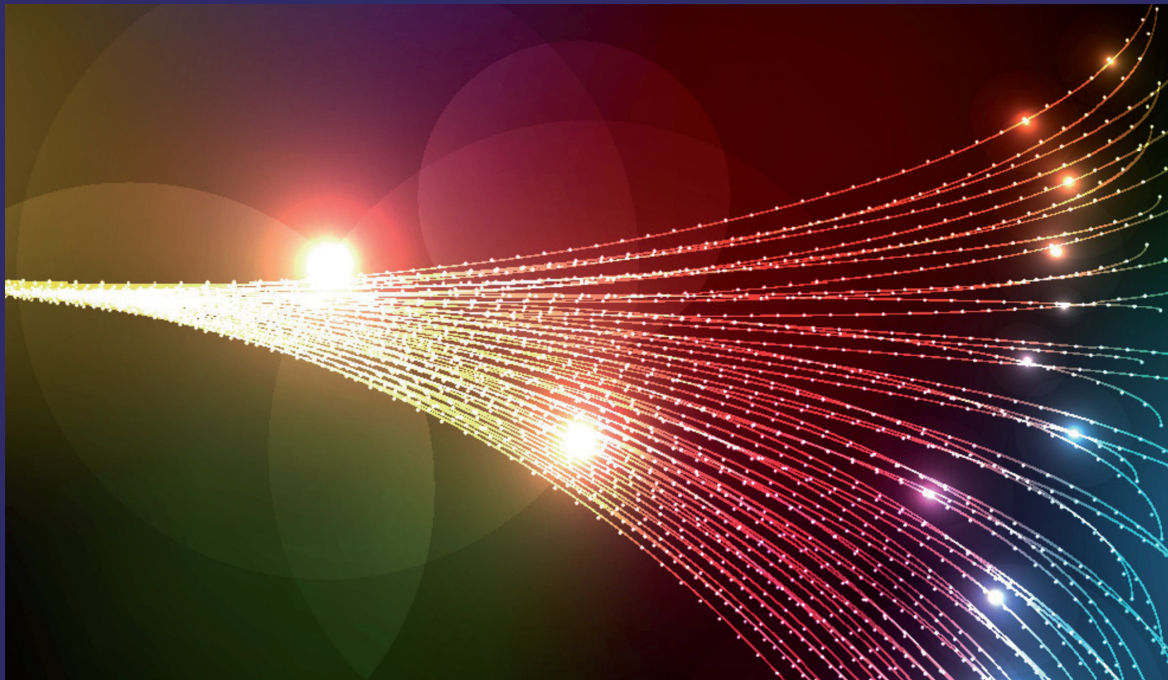
Sourav Mondal received the M.Tech in Telecommunication Systems Engineering from Indian Institute of Technology Kharagpur and the B.Tech in Electronics & Communication Engineering from Kalyani Govt. Engineering College, in 2014 and 2012, respectively. His thesis work was carried out in the G. S. Sanyal School of Telecommunications, IIT Kharagpur.



978-3-659-62542-8

Mondal

BER modeling of RSOA based LR-PON



Sourav Mondal

Long Reach RSOA based Passive Optical Networks

Sourav Mondal

Long Reach RSOA based Passive Optical Networks

Sourav Mondal

Long Reach RSOA based Passive Optical Networks

LAP LAMBERT Academic Publishing

Impressum / Imprint

Bibliografische Information der Deutschen Nationalbibliothek: Die Deutsche Nationalbibliothek verzeichnet diese Publikation in der Deutschen Nationalbibliografie; detaillierte bibliografische Daten sind im Internet über <http://dnb.d-nb.de> abrufbar.

Alle in diesem Buch genannten Marken und Produktnamen unterliegen warenzeichen-, marken- oder patentrechtlichem Schutz bzw. sind Warenzeichen oder eingetragene Warenzeichen der jeweiligen Inhaber. Die Wiedergabe von Marken, Produktnamen, Gebrauchsnamen, Handelsnamen, Warenbezeichnungen u.s.w. in diesem Werk berechtigt auch ohne besondere Kennzeichnung nicht zu der Annahme, dass solche Namen im Sinne der Warenzeichen- und Markenschutzgesetzgebung als frei zu betrachten wären und daher von jedermann benutzt werden dürften.

Bibliographic information published by the Deutsche Nationalbibliothek: The Deutsche Nationalbibliothek lists this publication in the Deutsche Nationalbibliografie; detailed bibliographic data are available in the Internet at <http://dnb.d-nb.de>.

Any brand names and product names mentioned in this book are subject to trademark, brand or patent protection and are trademarks or registered trademarks of their respective holders. The use of brand names, product names, common names, trade names, product descriptions etc. even without a particular marking in this works is in no way to be construed to mean that such names may be regarded as unrestricted in respect of trademark and brand protection legislation and could thus be used by anyone.

Coverbild / Cover image: www.ingimage.com

Verlag / Publisher:

LAP LAMBERT Academic Publishing
ist ein Imprint der / is a trademark of
OmniScriptum GmbH & Co. KG
Heinrich-Böcking-Str. 6-8, 66121 Saarbrücken, Deutschland / Germany
Email: info@lap-publishing.com

Herstellung: siehe letzte Seite /

Printed at: see last page

ISBN: 978-3-659-62542-8

Zugl. / Approved by: Kharagpur, Indian Institute of Technology, Diss., 2014

Copyright © 2014 OmniScriptum GmbH & Co. KG

Alle Rechte vorbehalten. / All rights reserved. Saarbrücken 2014

Contents

Contents	i – ii
List of Figures	iii – vi
List of Tables	vii
List of Abbreviations	viii
1. Introduction	1 – 9
1.1 Background	1
1.2 Literature Survey	4
1.2.1 Signal Power Compensation	5
1.2.2 Optical Source	6
1.2.3 Burst Mode Receiver	6
1.2.4 Upstream Resource Allocation	6
1.3 Motivation and Objectives	7
1.4 Organization of the Book	8
2. Architecture of Long Reach Passive Optical Network	10 – 13
2.1 Conventional Architecture	10
2.2 Proposed Architecture with CW lasers at OLT	11
2.3 Proposed Architecture with CW lasers near RN	12
2.4 Relative comparison among architectures	13
3. Reflective Semiconductor Optical Amplifier	14 – 34
3.1 Introduction	14
3.2 Steady-State modeling of RSOA	16
3.3 Algorithm for Numerical Solution of the Equations	23
3.4 Comparison of simulation results with a real device datasheet ratings	25
3.5 Results and Discussions	25
4. Arrayed Waveguide Grating	35 – 45
4.1 Introduction	35
4.2 Waveguide Layout and Basic Equations	36
4.3 Periodic Assignment of Wavelengths/Frequencies	37
4.4 Calculation of Signal Power at Output Ports of AWG	38
4.5 Calculation of Inter-channel Crosstalk at Output Ports	41
4.6 Results and Discussions	42
5. Erbium Doped Fiber Amplifier	46 - 63
5.1 Introduction	46
5.2 The fundamentals of EDFA	46
5.3 Three level amplification system	48
5.4 Three level to Two level reduced amplification system	51
5.5 Amplified Spontaneous Emission	54
5.6 Algorithm for Numerical Solution of the Equations	55
5.7 Comparison of simulation results with a real device datasheet ratings	57

5.8	Results and Discussions	57
6.	End-to-End Bit Error Rate (BER) Analysis	64 – 78
6.1	Introduction	64
6.2	Computation of all the noise components in the network	64
6.3	BER calculation with Conventional Receiver	65
6.4	BER calculation with Burst Mode Receiver (BMR)	68
6.4.1	Structure of Burst Mode Receiver	69
6.4.2	Analytical BER model for BMR	70
6.5	Results and Discussions	71
7.	Conclusion and Future Work	79 – 81
7.1	Conclusion	79
7.2	Scope of Future Work	81
7.2.1	End-to-end BER performance analysis in RSOA based hybrid TDM-WDM LR-PONs with Broadband Source (e.g., LED)	81
7.2.2	Scheduling and Resource Allocation in RSOA based hybrid TDM-WDM LR-PONs	81
8.	Appendix	82 – 83
A.	Single pass gain in SOA & Double pass gain in RSOA	82
9.	Bibliography	84 – 87

List of Figures

1.1	Traditional Telecom Network vs. Long Reach Passive Optical Network	3
1.2	Network simplification by removing SDH equipment in metro network and using a PON with extended backhaul	4
2.1	Block schematic of the architecture of conventional WDM-TDM hybrid LR-PON	10
2.2	Block schematic of the architecture of proposed RSOA based WDM-TDM hybrid LR-PON with CW lasers at OLT	11
2.3	Block schematic of the architecture of proposed RSOA based WDM-TDM hybrid LR-PON with CW lasers near RN	12
3.1	Spontaneous and Stimulated processes in a two-level photonic amplifier system	14
3.2	Heterogeneous buried-ridge RSOA structure	15
3.3	Piecewise linear model used for RSOA active region	23
3.4	Flow-chart of the algorithm for steady-state model for RSOA	24
3.5	Material gain of InGaAsP direct bandgap bulk-material vs. Wavelength	26
3.6	Material gain vs. Wavelength & carrier density	26
3.7	Material absorption coefficient (α) vs. carrier density (n)	27
3.8	RSOA predicted Fibre-to-fibre gain vs. Input power (P_{in}) at signal wavelength 1537.7 nm and bias current 80 mA	28
3.9	RSOA predicted Fibre-to-fibre gain vs. Bias current at signal wavelength 1537.7 nm and optical input power -25 dBm	28
3.10	RSOA predicted ASE output power vs. input power (P_{in}) at signal wavelength 1537.7 nm and bias current 80 mA	29
3.11	RSOA carrier density at signal wavelength 1537.7 nm and bias current = 80 mA & optical input power = - 40 dBm	29
3.12	RSOA forward propagating signal photon rate at signal wavelength 1537.7 nm and bias current = 80 mA & optical input power = - 40 dBm	30
3.13	RSOA backward propagating signal photon rate at signal wavelength 1537.7 nm and bias current = 80 mA & optical input power = - 40 dBm	30
3.14	RSOA forward propagating ASE photon rate at signal wavelength 1537.7 nm and bias current = 80 mA & optical input power = - 40 dBm	31
3.15	RSOA backward propagating ASE photon rate at signal wavelength 1537.7 nm and bias current = 80 mA & optical input power = - 40 dBm	31
3.16	RSOA carrier density at signal wavelength 1537.7 nm and bias current = 80 mA & optical input power = - 10 dBm	32

3.17	RSOA forward propagating signal photon rate at signal wavelength 1537.7 nm and bias current = 80 mA & optical input power = - 10 dBm	32
3.18	RSOA backward propagating signal photon rate at signal wavelength 1537.7 nm and bias current = 80 mA & optical input power = - 10 dBm	33
3.19	RSOA forward propagating ASE photon rate at signal wavelength 1537.7 nm and bias current = 80 mA & optical input power = - 10 dBm	33
3.20	RSOA backward propagating ASE photon rate at signal wavelength 1537.7 nm and bias current = 80 mA & optical input power = - 10 dBm	34
4.1	Schematic layout of Arrayed Waveguide Grating	35
4.2	AWG power profile at all the output ports for input power +3 dBm	42
4.3	AWG power profile at all the output ports for input power -6 dBm	43
4.4	AWG Loss characteristics at all the output ports for input power = +3 dBm	43
4.5	AWG Loss characteristics at all the output ports for input power = - 6 dBm	44
4.6	AWG inter-channel crosstalk at input power =+3 dBm	44
4.7	AWG inter-channel crosstalk at input power = -6 dBm	45
5.1	Erbium ion energy level diagram and corresponding spontaneous lifetime	47
5.2	Gain/loss spectra at different inversion levels for an erbium-doped fiber	47
5.3	Schematic diagram of a two-stage erbium-doped fiber amplifier for low noise figure and high output power operation	48
5.4	A typical three-level system used for amplifier model	49
5.5	Energy levels of a two-multiplet system, where state 3 is a higher lying state of multiplet 2	51
5.6	Gain characteristics of EDFA vs. wavelength for fibre length = 5m	58
5.7	Gain characteristics of EDFA vs. wavelength for fibre length = 10m	58
5.8	Single-pass gain of EDFA of different lengths vs. pump power at 980 nm	59
5.9	Small-signal gain of EDFA at 1550 nm vs. optical input power at pump = 980 nm, 40 mW	59
5.10	ASE output of EDFA at 1550 nm vs. optical input power at pump = 980 nm, 40 mW	60
5.11	Signal gain of a signal = 1550 nm, 50 μ W vs. pump power at 980 nm	60
5.12	ASE power generated with a signal = 1550 nm, 50 μ W vs. pump power at 980 nm	61
5.13	Amplification of a signal = 1550 nm, 50 μ W along the length of fibre	61
5.14	Distribution of Forward & Backward ASE with a signal = 1550 nm, 50 μ W along the length of fibre	62

5.15	Distribution of Meta-stable & ground carriers with a signal = 1550 nm, 50 μ W along the length of fibre	62
5.16	WDM gain on different wavelengths when total no. of channels = 16, signal power = -24.5 dBm, pump = 980 nm, 40 mW	63
5.17	WDM gain on different wavelengths when total no. of channels = 32, signal power = -24.5 dBm, pump = 980 nm, 40 mW	63
6.1	Flow diagram for considering all signal losses & amplification with ASE generation in the upstream for architecture with CW lasers at OLT	67
6.2	Flow diagram for considering all signal losses & amplification with ASE generation in the upstream for architecture with CW lasers near RN	68
6.3	The dynamic threshold variation of a BMR	69
6.4	(a) The PDF of symbols at receiver with conventional receiver, (b) The PDF of symbols at receiver with Burst Mode Receiver	69
6.5	Ideal feed-forward burst mode receiver with an integrating sample and hold for the determination of the proper threshold	70
6.6	Bit Error Rates on all 16 channels for input power = +3 dBm, reach = 10+10 Km & 16 users at a datarate = 1 Gbps	72
6.7	Bit Error Rates on all 16 channels for input power = +3 dBm, reach = 10+10 Km & 32 users at a datarate = 1 Gbps	72
6.8	Bit Error Rates on all 16 channels for input power = +3 dBm, reach = 40+10 Km & 16 users at a datarate = 1 Gbps	73
6.9	Bit Error Rates on all 16 channels for input power = +3 dBm, reach = 90+10 Km & 16 users at a datarate = 1 Gbps	73
6.10	Bit Error Rates on all 16 channels for input power = +3 dBm, reach = 20+10 Km & 16 users at a datarate = 1 Gbps with Burst Mode Receiver	74
6.11	Bit Error Rates on all 16 channels for input power = +3 dBm, reach = 40+10 Km & 16 users at a datarate = 1 Gbps with Burst Mode Receiver	74
6.12	Bit Error Rates on all 16 channels for input power = +3 dBm, reach = 10+10 Km & 16 users at a datarate = 1 Gbps	75
6.13	Bit Error Rates on all 16 channels for input power = +3 dBm, reach = 10+10 Km & 32 users at a datarate = 1 Gbps	76
6.14	Bit Error Rates on all 16 channels for input power = +3 dBm, reach = 40+10 Km & 16 users at a datarate = 1 Gbps	76
6.15	Bit Error Rates on all 16 channels for input power = +3 dBm, reach = 90+10 Km & 16 users at a datarate = 1 Gbps	77
6.16	Bit Error Rates on all 16 channels for input power = +3 dBm, reach = 20+10 Km & 16 users at a datarate = 1 Gbps with Burst Mode Receiver	77
6.17	Bit Error Rates on all 16 channels for input power = +3 dBm, reach = 40+10 Km & 16 users at a datarate = 1 Gbps with Burst Mode Receiver	78

7.1	Bit Error Rates of Best & Worst channels vs. reach of the RSOA based Long-Reach Passive Optical Network for architecture with CW lasers at OLT with input power = +3 dBm & 16 users at a datarate = 1 Gbps	79
7.2	Bit Error Rates of Best & Worst channels vs. reach of the RSOA based Long-Reach Passive Optical Network for architecture with CW lasers near RN with input power = +3 dBm & 16 users at a datarate = 1 Gbps	80
A.1	Light amplification in SOA	82
A.2	Light amplification in RSOA	83

List of Tables

1.1	Summary of different access technologies	2
1.2	Optical Amplifier technology comparison	5
3.1	RSOA geometrical and material parameters	19
3.2	Comparison between real device ratings & simulation results	25
4.1	Frequency assignment of the Arrayed Waveguide Grating (AWG)	38
5.1	EDFA geometrical and material parameters used in the steady-state model	54
5.2	Comparison between real device ratings & simulation results	56
6.1	Description of system parameters	66

List of Abbreviation

ASE	Amplified Spontaneous Emission
APON	ATM Passive Optical Network
ATM	Asynchronous Transfer Mode
AWG	Arrayed Waveguide Grating
BER	Bit Error Rate
BMR	Burst Mode Receiver
BPON	Broadband Passive Optical Network
CATV	Cable Television
CO	Central Office
DC	Direct Current
DSL	Digital Subscriber Line
DWDM	Dense Wavelength Division Multiplexing
EDFA	Erbium Doped Fiber Amplifier
EPON	Ethernet Passive Optical Network
FTTC	Fiber to the Curb
FTTH	Fiber to the Home
FTTP	Fiber to the Premises
Gbps	Giga bit per second
GPON	Gigabit Passive Optical Network
IPTV	Internet Protocol Television
LR	Long Reach
Mbps	Mega bit per second
OLT	Optical Line Terminal
ONU	Optical Network Unit
PON	Passive Optical Network
PSD	Power Spectral Density
RF	Radio Frequency
RIN	Relative Intensity Noise
RN	Remote Node
RSOA	Reflective Semiconductor Optical Amplifier
SOA	Semiconductor Optical Amplifier
TDM	Time Division Multiplexing
TDMA	Time Division Multiple Access
VoD	Voice on Demand
WDM	Wavelength Division Multiplexing

Chapter 1

Introduction

1.1 Background

The present explosive increase in demand for bandwidth in broadband access networks with the ongoing growth of communication networks is primarily because of the advent of bandwidth hungry multimedia services like Video-on-Demand (VoD), Internet Protocol Television (IPTV), video live streaming, video conferencing, online gaming and many more [1]. Telecom network architecture consists of backbone, regional, metro and access segments as shown in Fig. 1.1. The backbone network has grown rapidly due to its economic feasibility, but the access part remains extremely cost-sensitive. The current access technologies such as Digital Subscriber Line (DSL) and its variations cannot meet up this demand successfully, because of their limitation in bandwidth as well as coverage distance. A typical DSL provides downstream bandwidth 1.5 Mbps and upstream bandwidth 128 Kbps with coverage not more than 18,000 feet from Central Office (CO). A few variations of DSL, for example, very-high-bit-rate DSL (VDSL) can support downstream bandwidth of 50 Mbps, but, up to 1,500 feet only, G.SHDSL offers 2.3 Mbps in both directions, ADSL2 offers 12 Mbps and ADSL2+ offers 25 Mbps [2]. Another access technology, Cable Television (CATV) networks, which provide Internet services by dedicating some radio frequency (RF) channels in coaxial cables for data, but, as it is designed mainly for broadcasting, it doesn't fit very well for access networks [2]. So, the telecomm operators worldwide face a significant problem to deploy access networks that can support huge datarate and telephony services simultaneously and also has a large area of coverage. A brief summary of a few present access technologies are given in Table 1.1.

Traditional telecommunication network has high speed optical carriers in the backbone and in the regional/metro networks while copper based cables are used in access layer. These copper based cables do not support high bandwidth services. To

solve this issue, there evolved the technologies with a completely different architectures and capable enabling huge bandwidth (up to 100 Mbps per user) to the end users, are FTTx models — Fibre to the Home (FTTH), Fibre to the Curb (FTTC), Fibre to the Premises (FTTP) etc. and Passive Optical Network (PON) enables this bandwidth to be efficiently utilized [2]. PONs typically use tree-and-branch, ring-and-spur etc. point-to-multipoint topologies to share the resources among many users to reduce the Capital Expenditure (CapEx) and Operational Expenditure (OpEx), rather than providing a dedicated fibre to a single user [4]. Even if the fibre is not taken to home directly, it is taken very close to home premise and from there, technologies like DSL, Radio-over-Fibre (RoF) or any wireless service can take over, because of Microwave photonics, which integrates the radio-frequency engineering and optoelectronics [6]. Recently developed standards of PON include Ethernet PON (EPON), ATM PON (APON), Broadband PON (BPON), Gigabit PON (GPON) and wavelength division multiplexing PON (WDM-PON) etc. [2]. PON reduces the network cost by eliminating the power supply (operational cost) along the fiber path from Central Office (CO) to end users, and by sharing the network cost among multiple users, as shown in Fig. 1.1.

Table 1.1: Summary of different access technologies [3]

Access Technology	Downlink Bandwidth	Uplink Bandwidth	Coverage Distance
ADSL	1.5 – 6.1 Mbps	16 – 640 Kbps	12,000 ft on T1 line
ADSL Lite	1.5 Mbps	500 Kbps	18,000 ft on T1 line
HDSL	1.5 – 2.0 Mbps	1.5 – 2.0 Mbps	12,000 ft on T1 line
SDSL	768 Kbps	768 Kbps	12,000 ft on T1 line
VDSL	25 – 55 Mbps	3.2 Mbps	~ 10, 000 ft on coaxial /fibre optic cable
FTTx	~ 100 Mbps	~ 70 Mbps	1 – 20 Km, fibre optic cable

A standard PON has a maximum reach of 20 Km only and 16, 32 or 64 split-ratios for EPON, BPON or GPON, respectively. The prime reason for cost saving in PON is due to the replacement of synchronous digital hierarchy (SDH) rings with a single backhaul fibre, which reduces number of local exchanges, as shown in Fig. 1.2 [4]. But, still the reduction of cost offered by PON is not satisfactory enough to future telecom networks because of the expensive optical device that has to be installed at customer premises [8].

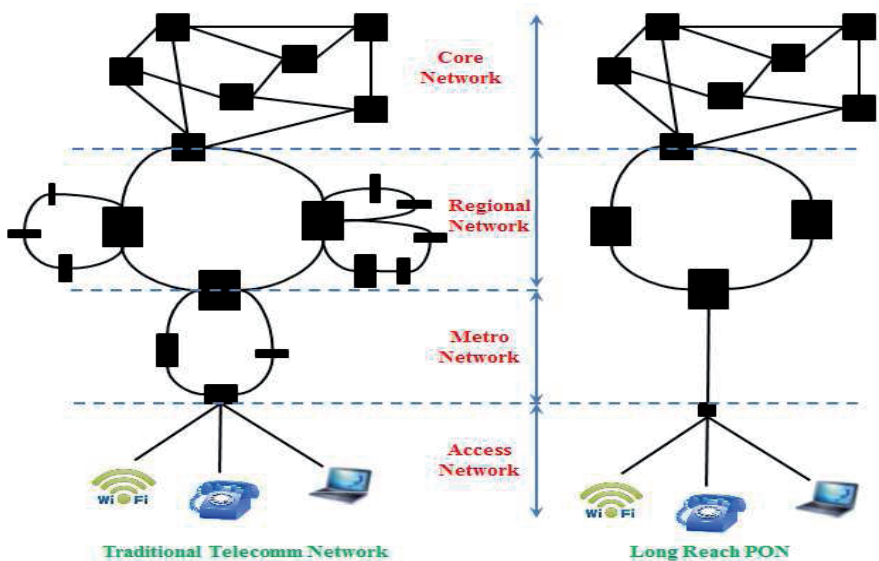


Fig. 1.1. Traditional Telecomm Network vs. Long Reach Passive Optical Network [2]

Thus, an alternative technology, known as Long Reach Passive Optical Network (LR-PON), has evolved. A number of long-reach optical access network architectures have been developed. Initially, the networks were single channel, where a single wavelength is shared between all users, using time division multiplexing (TDM). These networks were followed by wavelength division multiplexing systems that shared a number of wavelengths between groups of users. More recently, GPON extension systems have been developed that enable a number of existing GPONs to be grouped and converted into long-reach systems with dense wavelength division multiplexing (DWDM) backhaul systems. Thus, LR-PON promises sharing of resources among

1024 or more number of users by employing wavelength division multiplexing (WDM) and a reach of more than 100 Km, by using optical amplifiers like semiconductor optical amplifier (SOA), erbium-doped fibre amplifier (EDFA), Raman optical amplifier etc. [2].

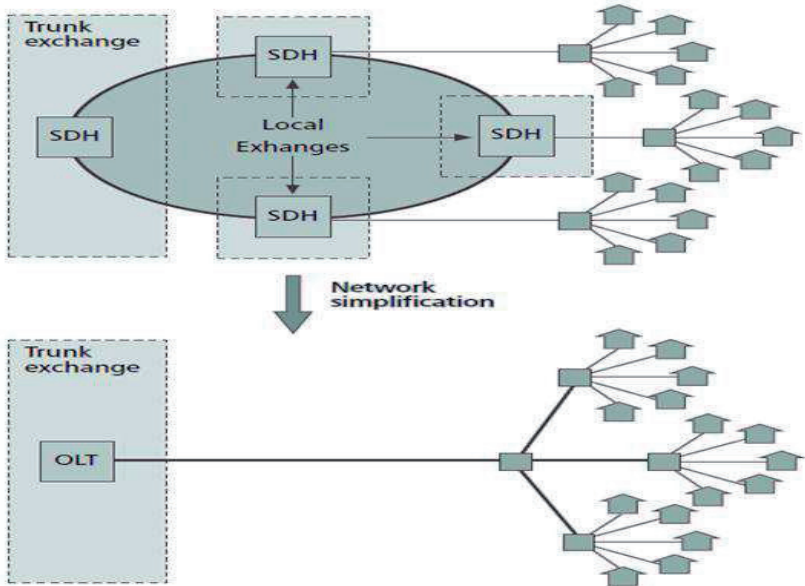


Fig. 1.2. Network simplification by removing SDH equipment in metro network and using a PON with extended backhaul [4]

1.2 Literature Survey

The LR-PON is not a fully passive solution because optical amplifiers are present at the remote node which requires pump sources. However, the LR-PON can be made passive by placing the pump sources for the amplifiers at the Central Office. Chapter 2 discusses about the general architecture of a LR-PON in detail. The central office (CO) connects the core network and the access network, and implements layer 2 and layer 3 functions, e.g., resource allocation, service aggregation, management, and control. The local exchange resides in the local users' area, which is close to the end customer equipment: ONU (within 10 km of drop section). The optical signal propagates across the fiber forming the feeder section (100 km and beyond) with the CO and the local

exchange at its two ends; then the fiber is split and connected to a large number of ONUs. In order to compensate for the power loss due to long transmission distance and high split size, optical amplifiers are used at the OLT and the local exchange. The different research challenges in LR-PON are as follows [2]:

1.2.1 Signal Power Compensation

Optical amplification is indispensable in an LR-PON. Besides amplifying the signal, the amplifiers introduce two challenges, as indicated below. Optical amplifiers have a detrimental effect on system performance because of unwanted noise, known as amplified spontaneous emission (ASE), a side effect of the amplification mechanism. As the high split of LR-PON would attenuate the signal significantly, the optical signal power could be sufficiently low at the input of the amplifier. As a result, the signal-to-noise ratio (SNR) could be reduced significantly because power budget remains constant.

In LR-PON due to the increased distance between optical line terminal (OLT) and the optical network units (ONUs) and other losses. The choices for the amplifiers are Erbium-doped fiber amplifier (EDFA), semiconductor optical amplifier (SOA) and Raman amplifiers. Comparisons between different optical amplifiers are shown in Table 1.2.

Table 1.2: Optical Amplifier technology comparison [1]

Amplifier	Gain (dB)	Optical Bandwidth (nm)	Noise Figure (dB)	Cost	Response time
EDFA	15 – 20	~ 35	6 – 8	Low	0.1 – 1 ms
SOA	15 – 20	30 – 60	6 – 10	Low	~ ns
Raman	10 – 15	~ 25	3 – 6	High	instantaneous

The EDFA features a low noise figure, a high power gain, and a wide working bandwidth, which enable it to be advantageous in an LR-PON employing WDM. But the relatively slow speed in adjusting its gain makes it disadvantageous due to the

bursty nature. of upstream TDMA traffic in LR-PON, where the optical amplifier needs to adjust its gain fast enough when packets with different DC levels pass through it, in order to output packets with uniform signal amplitude.

1.2.2 Optical Source

In order to lower the CapEx and OpEx, a standard PON chooses lower-cost uncooled transmitters in the ONU, because a major investment for an optical access network is the cost associated with installing an optical transmitter and receiver in the ONU at the customer premises. However, the uncooled transmitter is temperature dependent which in turn transmits wavelength with a possible drift of 20 nm. As no component in a standard PON is wavelength critical, the performance may be unaffected. But in an LR-PON which exploits WDM to satisfy huge amount of traffic, the wavelength drift become crucial, especially for certain components such as optical filters.

1.2.3 Burst Mode Receiver

The different ONU–OLT distances mean different propagation attenuations for signals from ONUs to the OLT, which in turn results in varied DC levels of bursty packets from ONUs at the OLT. The optical amplifier increases the difference of the DC level of upstream signals from different ONUs, which requires good design of burst-mode receivers at the OLT. In current PONs, a DC-coupled receiver is used which requires the receiver to decide the correct DC power threshold on a burst-by-burst basis. Problem occurs when the PON scales up in speed (10Gbps and beyond) and number of customers supported (up to 512 users could share the same channel).

1.2.4 Upstream Resource Allocation

In LR-PON, the end users and the central office (CO) (through which users are connected to the rest of the Internet) are separated by a significant distance, typically 100 km and beyond. Hence, control-plane delays are significant, so that various known scheduling algorithms for packet-based networks are difficult to apply directly. Therefore, efficient remote-scheduling algorithms need to be developed which overcome the large CO-user distance, which support different classes of service, and

which are scalable in terms of the number of users supported as well. This delay issue is particularly important since the delay budget in an access network is approximately 1–2 ms for real-time applications, and taking into account the coast-to-coast propagation delay (approximately 25 ms), which is much larger for global scales, and the persistence of hearing of the human ear and the persistence of vision of the human eye, both of which are in the range of a few tens of milliseconds.

1.3 Motivation and Objectives

In order to tackle few of these issues, the idea of reflective ONU evolved. In the LR-PON with reflective ONU, the upstream lasers, instead of individual ONUs, are placed at the OLT. These lasers transmit continuous wave signals, which travel all the way long to the ONUs along with the downstream wavelengths, where they are modulated, amplified and reflected back to travel all the way long to OLT. The reflective device, preferably, Reflective Semiconductor Optical Amplifier (RSOA), brings in several benefits over laser. First of all, the need for tunable laser is omitted, which makes the ONU “colourless” and secure the network from malicious users. The power requirement is much less for RSOA and cooling units are not required. But, along with these advantages, there comes some severe disadvantages too. The RSOA introduces very strong ASE noise for small signal power levels. The total accumulated noise at the receiver due to thermal noise, shot noise, ASE noise, inter-channel crosstalk and their beat noise components makes the network a noise based network and thus motivated to find the end-to-end Bit Error Rate (BER) with conventional and Burst Mode Receiver.

So, the main objective of this work is to examine the feasibility of LR-PON physical layer uplink setup consisting of reflective ONUs with due consideration to the BER performance in presence of realistic and non-ideal characteristics of optical and optoelectronic devices used in the setup. In order to meet the requirements for this objective, studies in the following broad areas have been carried out and reported in this book.

- Analytical steady-state modeling of Reflective Semiconductor Optical Amplifier (RSOA)
- Analytical steady-state modeling of Erbium-Doped Fiber Amplifier (EDFA)
- Analytical modeling of Arrayed Waveguide Grating (AWG)
- Final end-to-end BER performance analysis in RSOA based hybrid TDM-WDM Long-Reach Passive Optical Networks with conventional receiver
- Final end-to-end BER performance analysis in RSOA based hybrid TDM-WDM Long-Reach Passive Optical Networks with Burst Mode Receiver (BMR)

1.4 Organization of the Book

The rest of the book is organized as follows.

Chapter 2, at first, presents the broader schematic of a typical architecture of hybrid TDM-WDM Long-Reach Passive Optical Networks and explains its principle of operation [5]. Then, presents the broader schematic of two proposed architectures of RSOA based hybrid TDM-WDM Long-Reach Passive Optical Networks and then gives a relative comparison between the performances of the two architectures.

In Chapter 3, the detailed derivation of steady-state analytical device model of Semiconductor Optical Amplifier (SOA) by Connelly is explored and then it has been mapped to a similar model for RSOA, to find its characteristics like signal gain and output ASE power.

Chapter 4 presents the analytical model for AWG which gives the device parameters, wavelength routing equation, technique and expression to find the power at each output port and expressions for inter-channel crosstalk in different ports.

Chapter 5 presents the detailed derivation of the steady-state analytical model for EDFA which can be used for single wavelength as well as multiple wavelength (WDM) scenarios.

Chapter 6 develops the model for end-to-end bit error rate analysis of the upstream for RSOA based hybrid TDM-WDM LR-PON with conventional receiver at first and then extends it for Burst Mode Receiver.

Finally, Chapter 7 presents the concluding remarks on the various investigations carried out in the book and a brief discussion on future scope and possible extensions of the present work.

Chapter 2

Architecture of Long Reach Passive Optical Network

2.1 Conventional Architecture

Several LR-PON architectures have been studied, as reported in recent literature [2][4][5]. Fig. 2.1 shows a typical schematic of conventional WDM-TDM hybrid LR-PON.

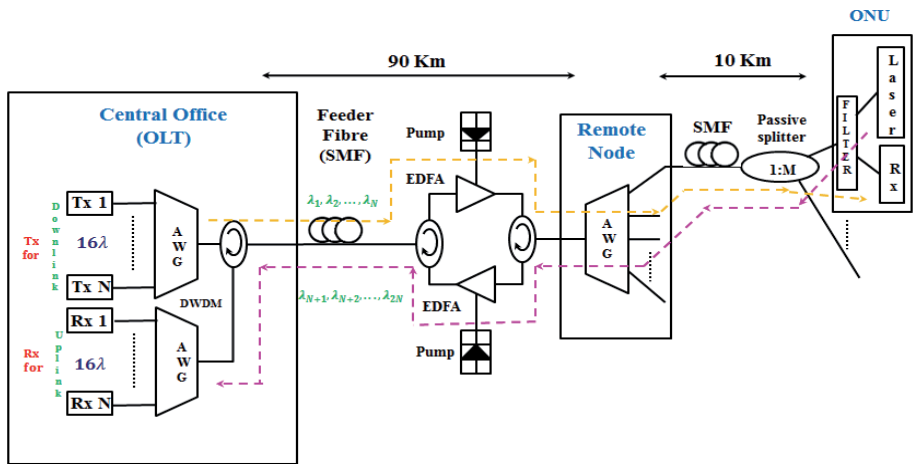


Fig. 2.1. Block schematic of the architecture of conventional WDM-TDM hybrid LR-PON

PON architecture. In the Central Office (CO) or Optical Line Terminal (OLT), there is a set of N downstream lasers having wavelengths $\lambda_1, \lambda_2, \dots, \lambda_N$, which are multiplexed, preferably by an Arrayed Waveguide Grating (AWG) or any optical multiplexer and are transmitted through the 90-100 Km long backhaul single mode fibre (SMF) to the Remote Node (RN). Just before RN, all the wavelengths are amplified by an EDFA. At RN, these wavelengths are again de-multiplexed by another AWG. Each of the wavelengths is passed through a $1:M$ passive splitter, so that they can be time division multiplexed among M end-user Optical Network Units (ONUs), around 5-10 Km away from the RN. Simultaneously, at each ONU, there is a laser for the upstream data transmission, having any one of the N wavelengths $\lambda_{N+1}, \lambda_{N+2}, \dots, \lambda_{2N}$, which are

multiplexed at RN and amplified by EDFA in the return path. Then these are transmitted through the backhaul fibre back to the OLT, where, they are de-multiplexed and detected by photo-detectors, say, Avalanche Photo-diode (APD) or PIN Photo-diode [5]. The wavelengths are primarily chosen in the C or L band.

2.2 Proposed Architecture with CW lasers at OLT

Now, the architectures proposed for RSOA based LR-PON have some additional features. In one possible architecture, as seen in Fig. 2.2, at the OLT, there is a set of

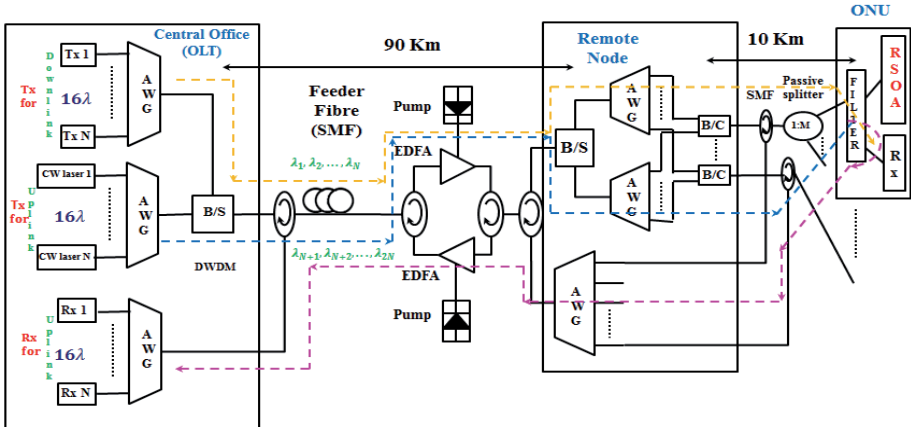


Fig. 2.2. Block schematic of the architecture of proposed RSOA based WDM-TDM hybrid LR-PON with CW lasers at OLT

N downstream lasers, as earlier, with another set of N CW lasers, which are to be used for upstream. The wavelengths containing downstream data and un-modulated carriers for upstream, are first multiplexed by two separate AWGs and then are combined using an optical band-combiner. These wavelengths are then transmitted through the 90-100 Km long backhaul single mode fibre (SMF) to the Remote Node (RN) like conventional architecture and just before RN, all the modulated downstream and un-modulated upstream wavelengths are amplified by an EDFA. At the remote node, the upstream and downstream wavelengths are separated by a band-splitter and are de-multiplexed by two separate AWGs. Then a corresponding pair of upstream and downstream wavelengths, say, $\lambda_1 \lambda_{N+1}, \lambda_2 \lambda_{N+2}$, and so on, are combined by an optical

band-combiner. After that, these are passed through a $1:M$ passive splitter, so that they can be time division multiplexed (TDM) among M end-user Optical Network Units (ONUs), around 5-10 Km away from the RN. The downstream λ_i is detected by photodetector and the upstream λ_j is modulated, amplified and reflected back by the RSOA. These reflected wavelengths are multiplexed at RN and then amplified by EDFA, as previous architecture. After this, they are transmitted back to the OLT through the backhaul fibre, where, they are de-multiplexed and detected by photo-detectors.

2.3 Proposed architecture with CW lasers near RN

Fig. 2.3 shows another possible architecture proposed, where the set of CW lasers for upstream are placed near the RN, just before the EDFA in forward path. This EDFA

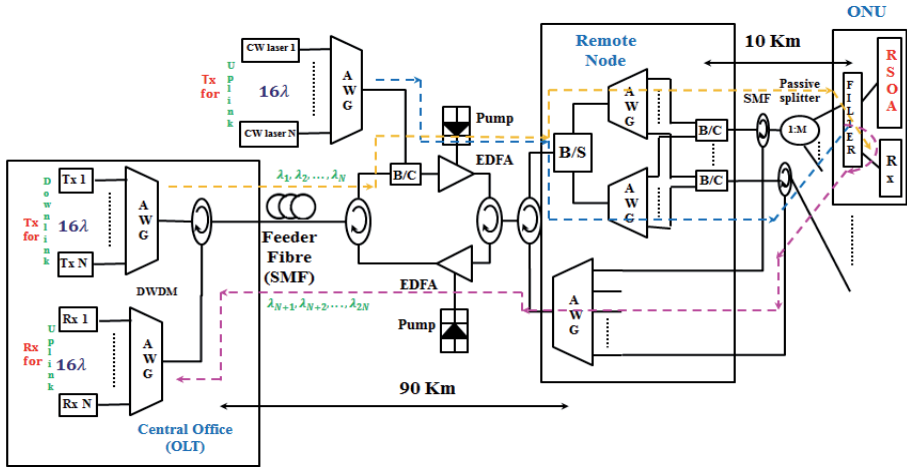


Fig. 2.3. Block schematic of the architecture of proposed RSOA based WDM-TDM hybrid LR-PON with CW lasers near RN

is preferred to have relatively smaller gain than the one in backward path. The rest is similar to architecture in Fig. 2.2. This keeps the signal power level before the EDFA high and thus, the total accumulated ASE noise power at the receiver is lesser and the end-to-end BER performance is expected to be a little better than the previous architecture.

2.4 Relative comparison among the architectures

In the conventional architecture, the upstream laser with additional cooling unit at the ONU makes the device costly to afford. But. Still they are designed to have a BER less than 10^{-9} for both downstream and upstream.

In the first architecture with CW lasers for upstream at OLT, the ONUs can be cheaper and no requirement of maintenance. But, this type of network becomes highly noise dominant network, because of the reflective device used, RSOA, which introduces huge amount of ASE noise for small signals. The two EDFAs also contribute to the ASE noise. Thus, the cheaper ONU comes at the cost of poorer BER.

In the second architecture, the CW lasers are placed near RN and the EDFA used in the forward path provides relatively smaller gain than previous architecture because signal is relatively stronger. As a result, the ASE introduced by first EDFA is also smaller. Thus, the performance of this type of architecture is expected to be little better than previous one.

So far, many architectures have been proposed for RSOA based LR-PON and many have performed small scale trials with this type of networks [9][10][11]. But, nowhere the detailed analytical end-to-end bit-error rate based performance analysis, along with the proper device modeling has been carried out, to the best of our knowledge. In this work, for the first time the steady-state analytical model for RSOA has been presented, “capture effect” in EDFA in WDM network scenario has been demonstrated and finally, considering all the loss and gain components in the network, the end-to-end bit-error rate analysis has been carried out, which can be extended for any architecture of RSOA based hybrid WDM-TDM LR-PON.

Chapter 3

Reflective Semiconductor Optical Amplifier

3.1 Introduction

The Reflective Semiconductor Optical Amplifier (RSOA) consists of conventional SOA (Semiconductor Optical Amplifier) in combination with a rear facet mirror such that the amplified light wave is retro-reflected. This feature of the RSOA provides high gain since the signal passes through the medium twice and also modulates the signal in accordance with the injection current, eliminating the need for light source.

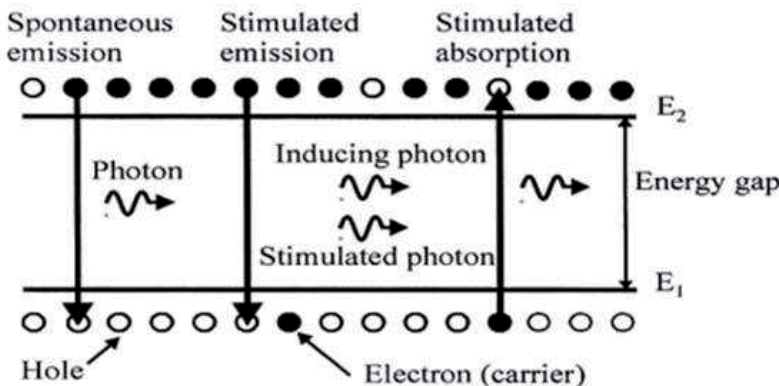


Fig. 3.1. Spontaneous and Stimulated processes in a two-level photonic amplifier system [13]

RSOA is a p-n junction device with one of the facet coated with anti-reflection material. The depletion region of the p-n junction device forms the active region. Light is amplified when it propagates through the active region of the p-n junction. The semiconductor material consists of two bands, viz., (i) a low mobility level valence band & (ii) a high mobility level conduction band. These two levels are separated by an energy difference called Energy gap E_g . No energy level exists in this energy-gap band. At thermal equilibrium, for a p-type semiconductor the concentration level of electron is very low in the conduction band. The energy of the electron in the valence

band is low and that of in the conduction band is high. In population inversion case the concentration of electrons in the conduction band is very high compared to valence band. Due to this increased concentration of electrons in the conduction band, in the presence of the optical signal, the transition of the electron from the higher energy level to the lower energy level (emission) takes place more than the transition of electron from lower energy level to higher energy level by absorption. Thus population inversion is one of the necessary conditions for optical gain [14].

The population inversion can be achieved by forward biasing the p-n junction. When no voltage is applied the concentration of the minority carriers is in their thermal equilibrium level. As forward bias voltage is applied the depletion region width reduces and carriers drift. The holes drift from p type to n-type and the electrons drift from the n-type to p-type. Thus population inversion takes place after a certain bias voltage and the device acts as an optical amplifier. In practice a thin layer of different semiconductor material (with higher refractive index and slightly smaller bandgap) is

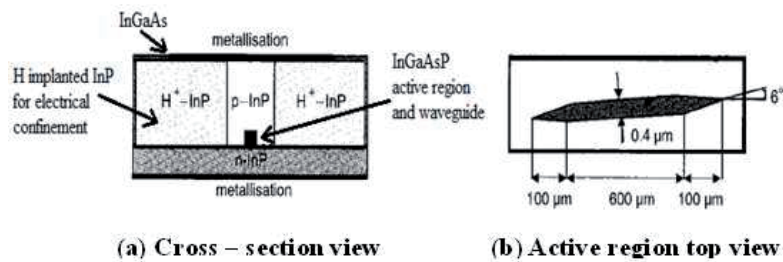


Fig. 3.2. Heterogeneous buried-ridge RSOA structure [13]

sandwiched between p and n type regions to confine the carriers injected into the active region and to confine the light during amplification. Such a device is called hetero-structure device, as shown in Fig 3.2.

Let us consider an optical frequency f_c such that $hf_c > E_g$ where E_g is the energy gap of the material. This optical amplifier can amplify signal with lowest frequency f_c . As the forward bias voltage is applied f_c is the first frequency to be amplified and as the

forward bias voltage is increased the signals with lower wavelengths or higher frequency can be amplified.

The rate of change of carrier density in RSOA is due to following processes, as shown in Fig. 3.1.

1. Increase in carrier density due to injection current
2. Radiative recombination
 - Spontaneous emission process
 - Stimulated emission process
3. Non radiative recombination

3.2 Steady-State modeling of RSOA

The particular RSOA device under consideration in this section is a $1.55 \mu\text{m}$ InP/In_{1-x} Ga_x As_yP_{1-y} homogeneous buried ridge stripe device. y and x are the molar fractions of Arsenide and Gallium respectively in the un-doped active region. Lattice matching is assumed for which $x = 0.47y$. The device structure consists of central active region of width W , thickness d and length L_c , as shown in Fig. 3.2.

The active region narrows linearly as a lateral taper of width W at the central region to zero width at each end. Each taper has length L_t . The tapers reduce the optical confinement factor from its maximum value Γ at the central active region to zero at the amplifier ends. This causes the guided mode lateral profile to expand which improves the input and output coupling efficiencies to single mode optical fibre.

As a first approximation the RSOA is modeled as a device of mean length L given by

$$L = L_c + L_t \quad (3.1)$$

with identical geometrical properties and optical confinement factor as the central active region. Geometrical and material parameters for the device under consideration are given in Table 3.1.

The InGaAsP direct bandgap bulk-material active region has a material gain coefficient g_m (m^{-1}) [15], given by

$$g_m(\nu, n) = \frac{c^2}{4\sqrt{2}\pi^{3/2}n_{\text{eff}}^2\tau\nu^2} \left(\frac{2m_e m_{hh}}{\hbar(m_e + m_{hh})} \right)^{3/2} \times \int_0^{\infty} \left[\sqrt{\nu' - \frac{E_g(n)}{\hbar}} (f_c(\nu) - f_v(\nu)) \right. \\ \left. \times \left(\frac{2T_0}{1 + (2\pi T_0)^2 (\nu' - \nu)^2} \right) \right] d\nu' \quad (3.2)$$

where,

c	Speed of light in vacuum;
ν	Optical frequency;
n_{eff}	Active region effective refractive index;
τ	Radiative carrier recombination lifetime;
\hbar	Planck's constant \hbar divided by 2π ;
m_e, m_{hh}	Conduction band (CB) electron and valence band (VB) heavy hole effective mass, respectively;
n	CB carrier (electron) density;
T_0	Mean lifetime for coherent interaction of electrons with a monochromatic field and is of the order of 1 ps

The bandgap energy can be expressed by, $E_g(n) = E_{g0} - eK_g n^{1/3}$ where K_g is the bandgap shrinkage coefficient. The main effect of bandgap shrinkage is to shift the peak of the gain and spontaneous emission spectra towards longer wavelengths. E_{g0} , the bandgap energy with no injected carriers, is given by the quadratic approximation,

$$E_{g0} = e(a + by + cy^2) \quad (3.3)$$

where a, b and c are the quadratic coefficients and e is electronic charge.

The Fermi-Dirac distributions in the CB and VB are given by

$$f_c(E) = \frac{1}{1 + \exp\left(\frac{E - E_{f_c}}{kT}\right)} \quad (3.4)$$

$$f_v(E) = \frac{1}{1 + \exp\left(\frac{E - E_{f_v}}{kT}\right)} \quad (3.5)$$

where,

$$E_a = (hv - E_g) \frac{m_{hh}}{m_c + m_{hh}} \quad (3.6)$$

$$E_b = -(hv - E_g) \frac{m_c}{m_c + m_{hh}} \quad (3.7)$$

where, T is absolute temperature and k is the Boltzmann constant.

E_{f_c} is the quasi-Fermi level of the CB relative to the bottom of the band. E_{f_v} is the quasi-Fermi level of the VB relative to the top of the band. They can be estimated using the Nilsson approximation [16],

$$E_{f_c} = \left\{ \ln \delta + \delta \left[64 + 0.05524 \delta (64 + \sqrt{\delta}) \right]^{-\frac{1}{4}} \right\} kT \quad (3.8)$$

$$E_{f_v} = - \left\{ \ln \varepsilon + \varepsilon \left[64 + 0.05524 \varepsilon (64 + \sqrt{\varepsilon}) \right]^{-\frac{1}{4}} \right\} kT \quad (3.9)$$

where,

$$\delta = \frac{n}{n_c} \text{ and } \varepsilon = \frac{p}{n_v} \quad (3.10)$$

With the assumption of Lorentzian Laser spectrum, we can make the following substitution in the expression for $g_m(m^{-1})$, in equation 3.2,

$$\left(\frac{2T_0}{\left(1 + (2\pi T_0)^2 (\nu' - \nu)^2 \right)} \right) = \delta(\nu - \nu') \quad (3.11)$$

as this function has a much narrower spectrum than the other terms within the integral. Hence, we obtain,

$$g_m(\nu, n) = \frac{c^2}{4\sqrt{2}\pi^{3/2}n_{eff}^2\tau\nu^2} \left(\frac{2m_e m_{hh}}{\hbar(m_e + m_{hh})} \right)^{3/2} \times \sqrt{\nu - \frac{E_g(n)}{\hbar}} (f_c(\nu) - f_v(\nu)) \quad (3.12)$$

Table 3.1: RSOA geometrical and material parameters [13]

Symbol	Parameter	Value
y	Molar fraction of Arsenide in the active region	0.892
L_c	Central active region length	600 μm
L_t	Tapered active region length	100 μm
d	Active region thickness	0.4 μm
W	Central active region width	0.4 μm
Γ	Optical confinement factor	0.45
K_g	Bandgap shrinkage coefficient	$0.9 \times 10^{-10} \text{ eVm}$
n_{eff}	Effective refractive index at zero carrier density	3.22
η_{in}	Input coupling loss	3.0 dB
η_{out}	Output coupling loss	3.0 dB
R_1	Input facet power reflectivity	10^{-6}
R_2	Output facet power reflectivity	0.99
A_{rad}	Linear radiative recombination coefficient	$1.0 \times 10^7 \text{ s}^{-1}$
B_{rad}	Bimolecular radiative recombination coefficient	$5.6 \times 10^{-16} \text{ m}^3 \text{s}^{-1}$
A_{nrad}	Linear non-radiative recombination coefficient	$3.5 \times 10^8 \text{ s}^{-1}$
B_{nrad}	Bimolecular non-radiative recombination coefficient	$0.0 \times 10^{-16} \text{ m}^3 \text{s}^{-1}$
C_{aug}	Auger recombination coefficient	$3.0 \times 10^{-41} \text{ m}^6 \text{s}^{-1}$
D_{leak}	Leakage recombination coefficient	$0.0 \times 10^{48} \text{ m}^{13.5 \text{s}^{-1}}$
a	Bandgap energy quadratic coefficient	1.35
b	Bandgap energy quadratic coefficient	-0.775
c	Bandgap energy quadratic coefficient	0.149
m_e	Effective mass of electron in the CB	$4.10 \times 10^{-32} \text{ kg}$
m_{hh}	Effective mass of a heavy hole in the VB	$4.19 \times 10^{-31} \text{ kg}$
m_{lh}	Effective mass of a light hole in the VB	$5.06 \times 10^{-32} \text{ kg}$
$P_{o,sat}$	Saturation output power	2 – 5 dBm

The material loss coefficient α (m^{-1}) is modeled as a linear function of carrier density as follows [17][18],

$$\alpha = \alpha_b + k_n n + k_p p \quad (3.13)$$

where, the small background loss coefficient α_b represents carrier density independent mechanisms like photon scattering at defects. Free-carrier absorption due to electrons is known to be negligible in $1.55 \mu\text{m}$ InGaAsP/InP devices ($k_n = 10^{-18} \text{ cm}^2$). Mainly holes dominate the absorption and gives $k_p = 82 \times 10^{-18} \text{ cm}^2$.

In the model, N_s signals are injected with optical frequencies ν_k ($k = 1 \dots N_s$) and power $P_{in,k}$ before coupling loss. The signals enter through front facet, travel through the amplifier, aided by the embedded waveguide, get reflected at the rear facet, again travel back through the amplifier similarly and exit at the front facet. In the following analysis it is assumed that transverse variations (i.e. normal to the propagation direction) in the photon rates and carrier density are negligible. This is a valid assumption because most SOA/RSOAs have a narrow active region. In the model the left and right facets have power reflectivities $R_1 \approx 0$ and $R_2 \approx 1$, respectively. The active region is split averagely into M subsections with $\Delta l = L / M$. The expression for material gain, as obtained earlier is needed to be modified because of the gain saturation, as follows [19]:

$$g_{m,new} = \frac{g_m}{1 + \frac{P_{out}}{P_{o,sat}}} \quad (3.14)$$

Now, the travelling-wave equations for the signal power in positive and negative z-directions are as follows [12][19],

$$\frac{dP_{s,k}^+(z)}{dz} = +\frac{1}{2}(\Gamma g_{m,new}(\nu_k, n) - \alpha(n)) P_{s,k}^+(z) \quad (3.15)$$

$$\frac{dP_{s,k}^-(z)}{dz} = -\frac{1}{2}(\Gamma g_{m,new}(\nu_k, n) - \alpha(n)) P_{s,k}^-(z) \quad (3.16)$$

with initial condition, $P_{in,k} = P_{in}(\nu_k) / \eta_{in}$ and the following boundary conditions,

$$\begin{aligned} P_{s,k}^+(0) &= (1 - R_1) P_{in,k} + R_1 P_{s,k}^-(0) \\ P_{s,k}^-(L) &= R_2 P_{s,k}^+(L) \end{aligned} \quad (3.17)$$

Solving the above differential equations, we finally obtain for RSOA,

$$P_{out_k}^{sig} = (1 - R_2) P_{s,k}^+(L) / \eta_{out} \quad (3.18)$$

The amplification of the signal also depends on the amount of spontaneously emitted noise generated by the amplifier. This is because the noise power takes part in draining the available carrier population and helps saturate the gain. However, it is not necessary to treat the spontaneous emission as a coherent signal since it distributes itself continuously over a relatively wide band of wavelengths with random phases between adjacent wavelength components.

The spontaneous emission photon rates N_j^+ and N_j^- (s^{-1}) with a particular polarization (TE or TM) in a frequency spacing $K_m \Delta \nu_m$ centred on frequency ν_j travelling in the positive and negative directions along the amplifier axis respectively obey the travelling-wave equations [12]

$$\frac{dN_j^+(z)}{dz} = +(\Gamma g_{m,new}(\nu_j, n) - \alpha(n)) N_j^+ + R_{sp}(\nu_j, n) \quad (3.19)$$

$$\frac{dN_j^-(z)}{dz} = -(\Gamma g_{m,new}(\nu_j, n) - \alpha(n)) N_j^- - R_{sp}(\nu_j, n) \quad (3.20)$$

subject to the boundary conditions

$$N_j^+(0) = R_1 N_j^-(0) \quad (3.21)$$

$$N_j^-(L) = R_2 N_j^+(L) \quad (3.22)$$

$R_{sp}(\nu_j, n)$ represents the spontaneous emission coupled into N_j^+ and N_j^- . An expression for R_{sp} can be derived by a comparison between the noise output from an ideal amplifier obtained by comparing above equations with the quantum mechanically derived expression [13] as follows:

$$R_{sp}(v_j, n) = (\Gamma g_{m,new}(v_j, n) - \alpha(n)) K_m \Delta v \quad (3.23)$$

where K_m is an integer ($= 20$) and Δv is inter-channel spacing in frequency domain (~ 100 GHz for 0.8 nm separated WDM channels in 1550 nm window).

Solving the above differential equations, we finally obtain for RSOA,

$$P_{out_k}^{ASE} = h v_j (1 - R_i) N_j^-(0) / \eta_{in} \quad (3.24)$$

The amplifier material gain and spontaneous emission originate from carriers injected into the active region by the bias current. The carrier density (m^{-3}) at position z in the amplifier obeys the rate equation give as follows [12]:

$$\begin{aligned} \frac{dn(z)}{dt} = & \frac{I}{edLW} - R(n(z)) - \frac{\Gamma}{dW} \left\{ \sum_{k=1}^{N_m} g_{m,new}(v_k, n) [N_{s_k}^+(z) + N_{s_k}^-] \right\} \\ & - \frac{2\Gamma}{dW} \left\{ \sum_{j=1}^{N_m} g_{m,new}(v_j, n) [N_j^+(z) + N_j^-] \right\} \end{aligned} \quad (3.25)$$

where I is the amplifier bias current. In above equation, all of the bias current is assumed to pass through the active region and not the surrounding InP regions. The bias current is assumed to have a uniform distribution across the active region width. The first term on the RHS of above equation represents the addition of carriers to the active region from the bias current. These injected carriers are then depleted by various mechanisms occurring within the amplifier. The second term is due to radiative and nonradiative recombination mechanisms, as follows:

$$\begin{aligned} R(n) &= R_{rad}(n) + R_{nrad}(n) \\ R_{rad}(n) &= A_{rad}n + B_{rad}n^2 \\ R_{nrad}(n) &= A_{nrad}n + B_{nrad}n^2 + C_{aug}n^3 + D_{leak}n^{5.5} \end{aligned} \quad (3.26)$$

It is assumed that carrier leakage from the active region into surrounding InP regions is negligible. The third and fourth terms on the RHS of rate equation represent radiative recombination of carriers due to the amplified signal photons ($N_{s_k}^\pm$) and ASE photons (N_j^\pm)

N_j^{\pm}). is included as only this fraction of amplified photons resides in the active region. The factor of two in rate equation accounts for the fact that spontaneously emitted photons can exist in one of two mutually orthogonal polarizations (TE or TM). In the

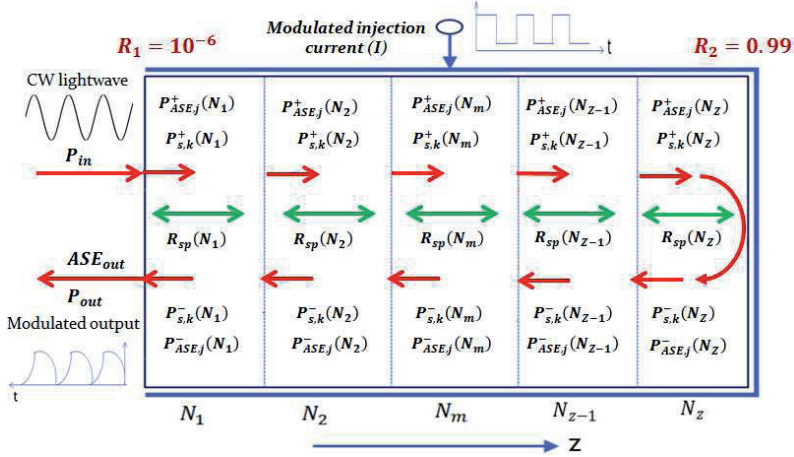


Fig. 3.3. Piecewise linear model used for RSOA active region [19]

model the SOA is assumed to be polarization independent. Polarization dependence can be included by the use of different TE and TM confinement factors.

3.3 Algorithm for Numerical Solution of the Equations

All these differential equations are needed to be solved numerically, as analytical solution is difficult to find. The total active region is divided into N_z sub-sections, labeled $i = 1$ to N_z and these equations are solved for each of the sections putting their corresponding boundary conditions, as shown in Fig. 3.3. At the steady-state, the RHS of rate equation (3.25), $Q(i)$, for each section, is equal to zero. Thus, to obtain the steady-state characteristics, an algorithm, based on the algorithm in[12], which uses the signal and ASE noise powers at the section boundaries, to adjust the carrier density through the active region so that $Q(i)$ remains close to zero, as much as possible.

The steps of the algorithm are described as follows:

Step – 1: Initialize the signal and spontaneous emission powers inside device to zero. The initial carrier density is obtained from the solution of rate equation (22), with signal & ASE photon rates set to zero.

Step – 2: The iteration now begins. The coefficients of the traveling-wave equations (3.15), (3.16), (3.19) and (3.20), are computed.

Step – 3: The signal and noise powers are estimated using finite difference solutions of travelling-wave equations for signal power and ASE. Forward differences are used for positive traveling-waves and backward differences for negative traveling-waves.

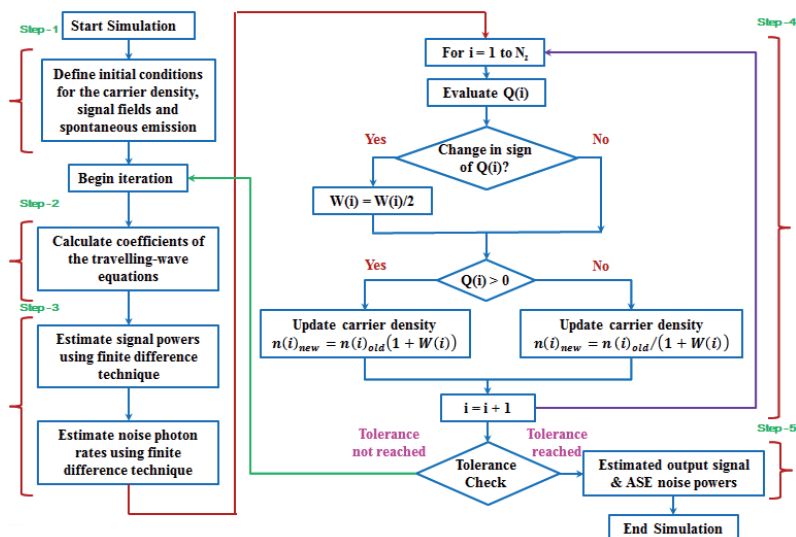


Fig. 3.4. Flow-chart of the algorithm for steady-state model for RSOA

Step – 4: $Q(i)$ is calculated for each section.

Positive value of $Q(i)$ implies the carrier density is too low and hence, the new value of carrier density for the section is increased by a factor $1 + W(i)$, where, $W(i)$ is a weight less than unity, preferably around 0.1.

Negative value of $Q(i)$ implies the carrier density is too high and hence, the new value of carrier density for the section is decreased by a factor $1 + W(i)$.

Meanwhile, if the sign of $Q(i)$ gets altered from the previous iteration, $W(i)$ is halved.

Step – 5: The iteration continues until the percentage change in the signal and noise powers and carrier density throughout the RSOA between successive iterations is less than the desired tolerance.

When the iteration stops, parameters such as signal gain and output spontaneous noise power are calculated. A flow chart for the algorithm is shown in Fig. 3.4.

A sample MATLAB code for this model is available in the following link:

<http://www.mathworks.in/matlabcentral/fileexchange/48262-reflective-semiconductor-optical-amplifier--rsoa--model>

3.4 Comparison of simulation results with a real device datasheet ratings

For the RSOA modeling, the steady-state wideband model of SOA proposed by M. J. Connelly [13] was studied and then based on the same model, the necessary changes were made to map it to RSOA. The simulation results were found to be very close to real RSOA devices. A comparison between the simulation results and ratings of a real device from datasheet [20] is given in Table 3.2.

Table 3.2: Comparison between real device ratings & simulation results

Parameter	Test Condition	Datasheet Rating	From simulation	Unit
Peak Gain Wavelength	80 mA & 20 °C	1540	1537.7	nm
Small Signal Gain	80 mA & 20 °C	25	25.6	dB
Saturated Output Power	80 mA & 20 °C Pin = -20 dBm	2	2	dBm
Integrated ASE Power	80 mA & 20 °C	3	3.16	mW
Maximum Drive Current	Across temp. range	100	130	mA
Maximum Optical I/P Power	80 mA & 20 °C	+13	+10	dBm
Front Facet Reflectivity	80 mA & 20 °C	< 10 ⁻⁵	10 ⁻⁶	-

3.5 Results and Discussions

The material gain of InGaAsP device used for RSOA varies with wavelength as shown in Fig. 3.5 and the gain increases proportionally with carrier density.

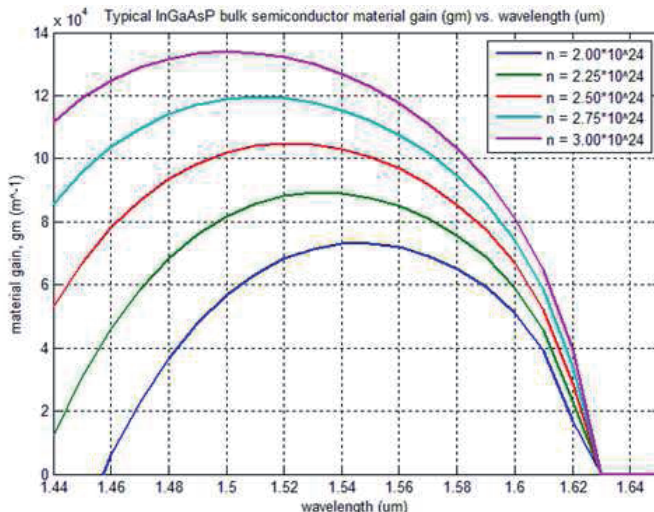


Fig. 3.5. Material gain of InGaAsP direct bandgap bulk-material vs. Wavelength

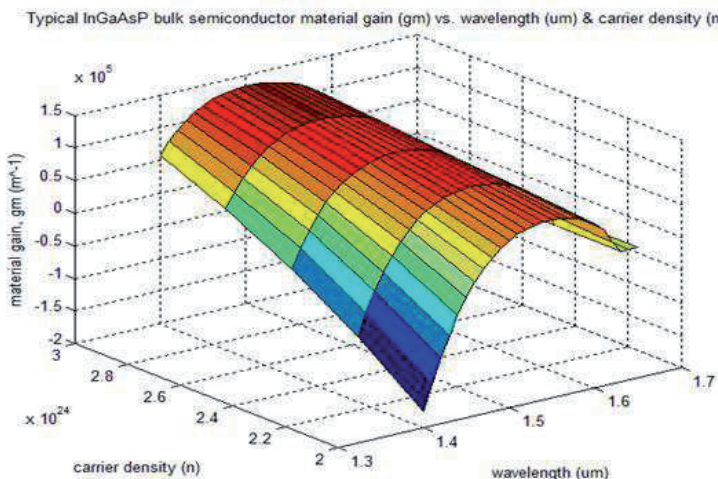


Fig. 3.6. Material gain vs. Wavelength & carrier density

The material absorption coefficient (α) varies with the carrier density as shown in Fig. 3.7.

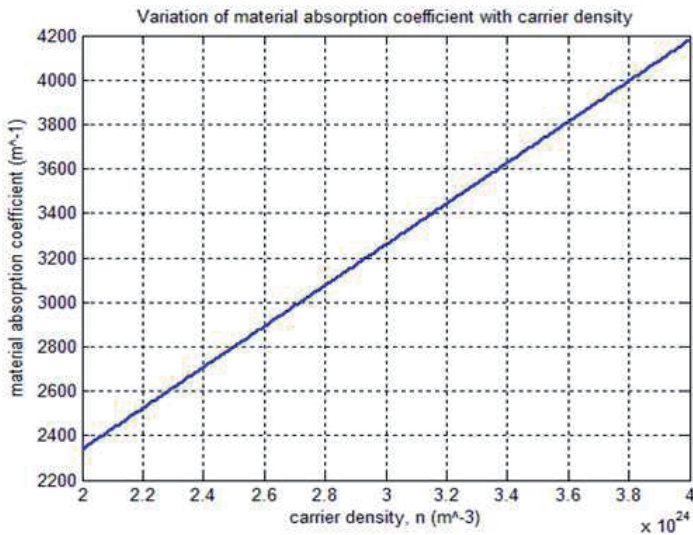


Fig. 3.7. Material absorption coefficient (α) vs. carrier density (n)

Fig. 3.8 shows the fiber-to-fiber gain of RSOA vs. input power at signal wavelength 1537.7 nm and a bias current 80 mA, where we can observe a gain saturation effect for signal power lesser than -20 dBm. Fig. 3.9 shows the fiber-to-fiber gain of RSOA vs. bias current, when the input power is fixed at -25 dBm at a wavelength of 1537.7 nm, where the gain saturates for bias current more than 80 mA. Fig. 3.10 shows the total ASE output power vs. input power at signal wavelength 1537.7 nm and a bias current 80 mA. Fig. 3.11 to 3.16 shows the carrier density distribution, forward signal power, backward signal power, forward ASE power and backward ASE power, respectively, when the input power is fixed at -40 dBm at a wavelength of 1537.7 nm. Similarly, Fig. 3.17 to 3.20 shows the carrier density distribution, forward signal power, backward

signal power, forward ASE power and backward ASE power, respectively, when the input power is fixed at -10 dBm at a wavelength of 1537.7 nm.

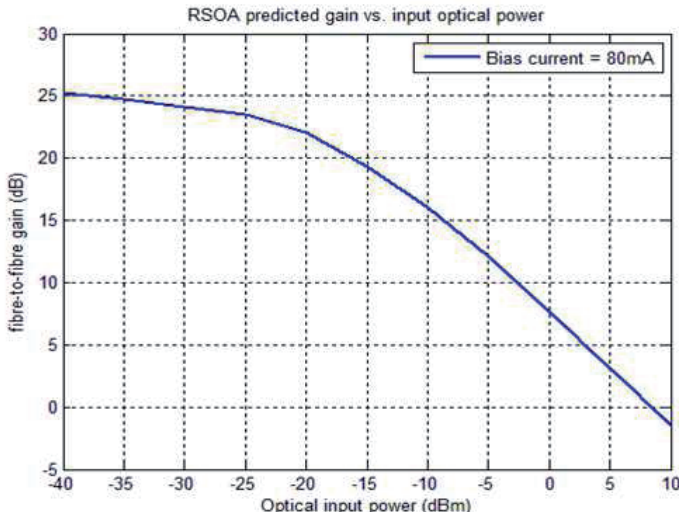


Fig. 3.8. RSOA predicted Fibre-to-fibre gain vs. Input power (P_{in}) at signal wavelength 1537.7 nm and bias current 80 mA

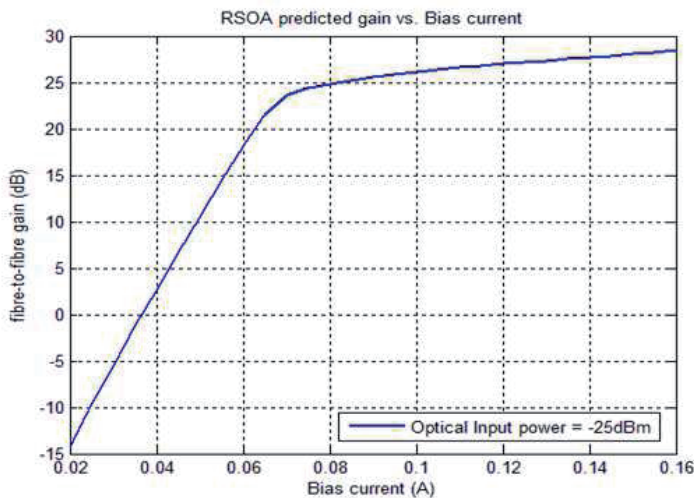


Fig. 3.9. RSOA predicted Fibre-to-fibre gain vs. Bias current at signal wavelength 1537.7 nm and optical input power -25 dBm

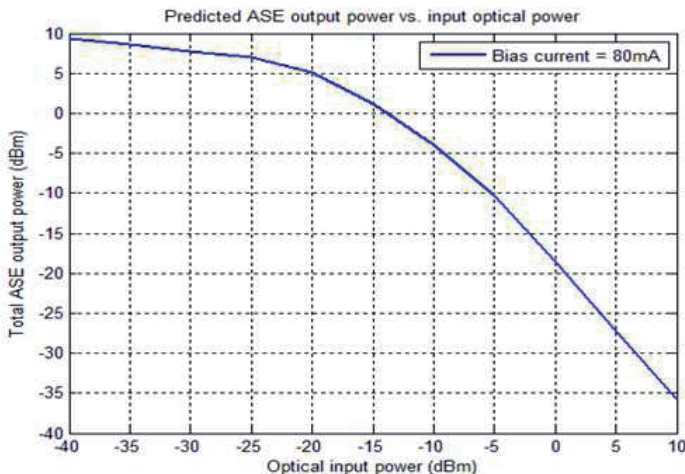


Fig. 3.10. RSOA predicted ASE output power vs. input power (P_{in}) at signal wavelength 1537.7 nm and bias current 80 mA

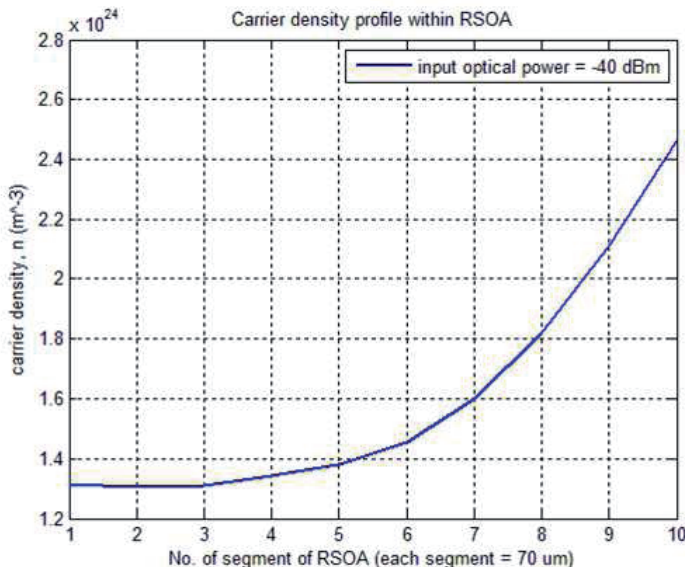


Fig. 3.11. RSOA carrier density at signal wavelength 1537.7 nm and bias current = 80 mA & optical input power = - 40 dBm

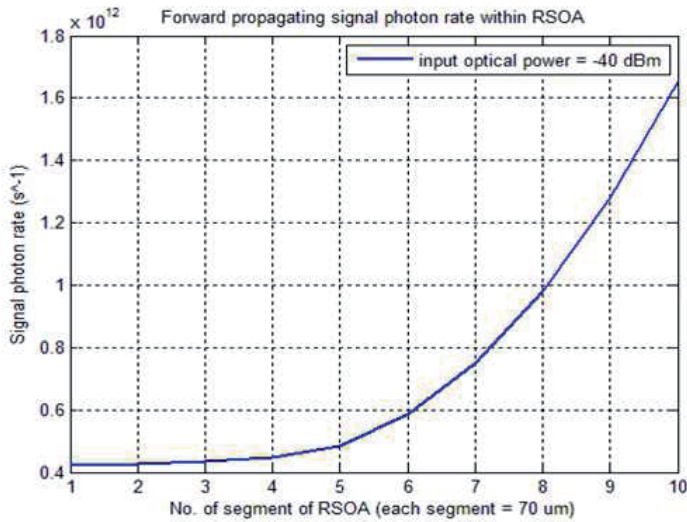


Fig. 3.12. RSOA forward propagating signal photon rate at signal wavelength 1537.7 nm and bias current = 80 mA & optical input power = - 40 dBm

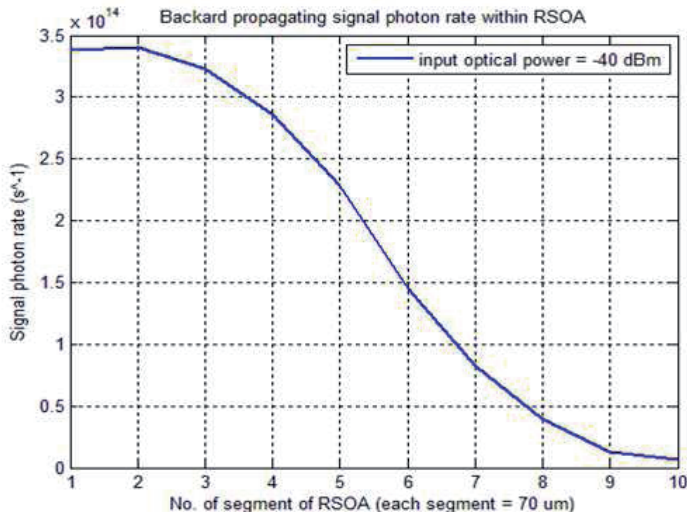


Fig. 3.13. RSOA backward propagating signal photon rate at signal wavelength 1537.7 nm and bias current = 80 mA & optical input power = - 40 dBm

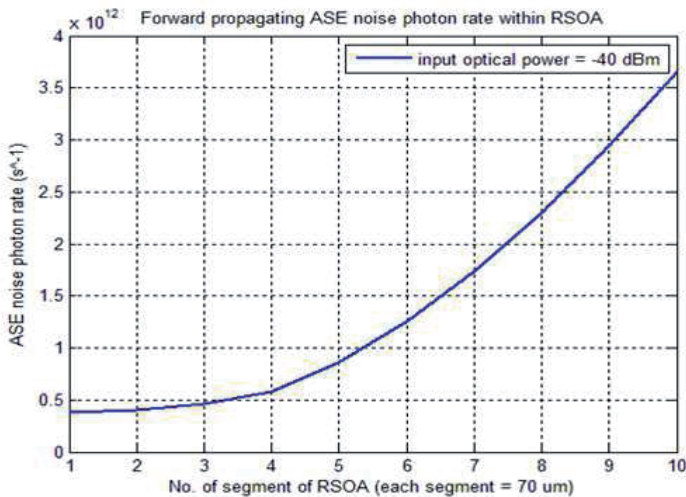


Fig. 3.14. RSOA forward propagating ASE photon rate at signal wavelength 1537.7 nm and bias current = 80 mA & optical input power = - 40 dBm

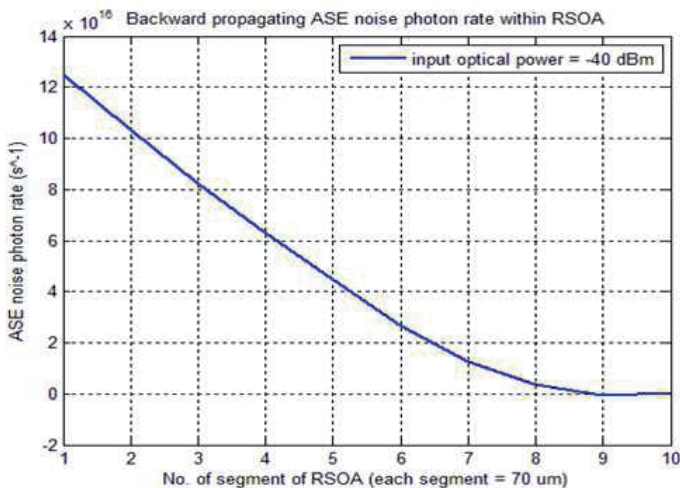


Fig. 3.15. RSOA backward propagating ASE photon rate at signal wavelength 1537.7 nm and bias current = 80 mA & optical input power = - 40 dBm

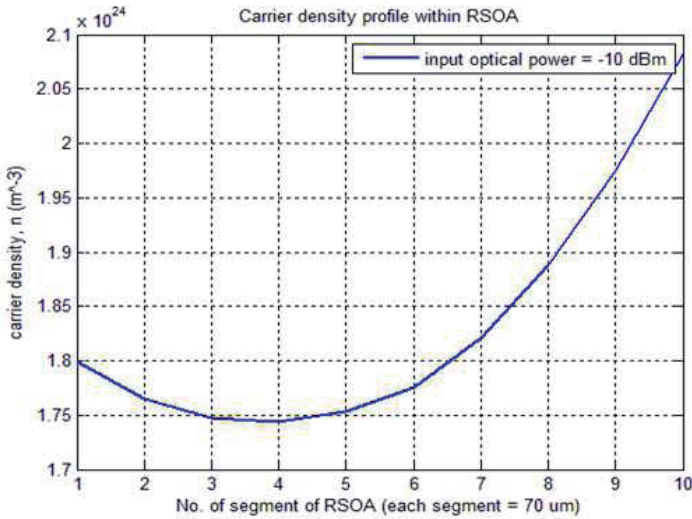


Fig. 3.16. RSOA carrier density at signal wavelength 1537.7 nm and bias current = 80 mA & optical input power = - 10 dBm

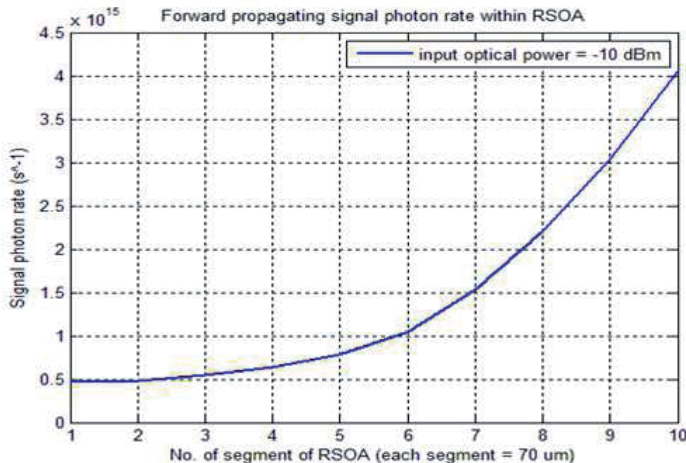


Fig. 3.17. RSOA forward propagating signal photon rate at signal wavelength 1537.7 nm and bias current = 80 mA & optical input power = - 10 dBm

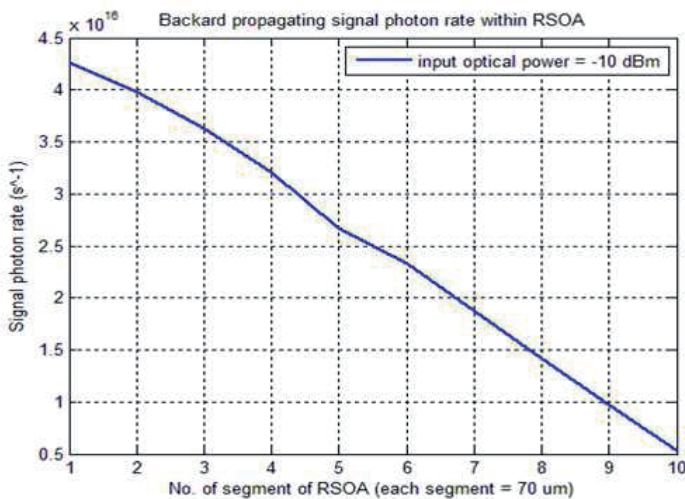


Fig. 3.18. RSOA backward propagating signal photon rate at signal wavelength 1537.7 nm and bias current = 80 mA & optical input power = - 10 dBm

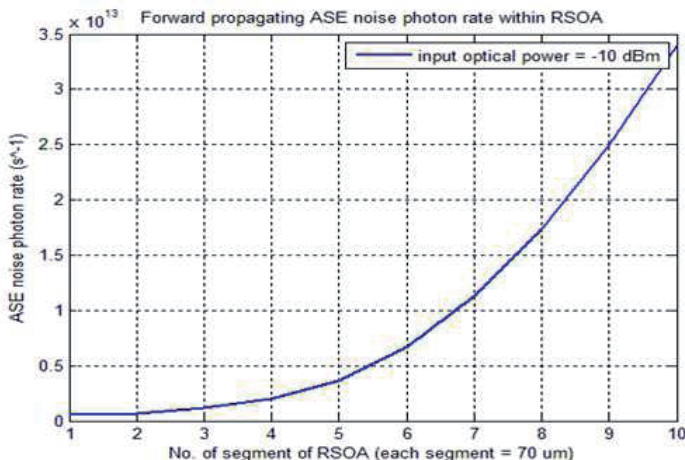


Fig. 3.19. RSOA forward propagating ASE photon rate at signal wavelength 1537.7 nm and bias current = 80 mA & optical input power = - 10 dBm

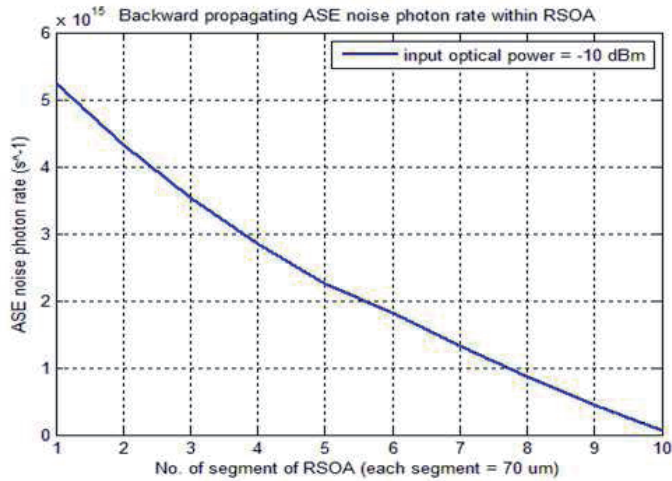


Fig. 3.20. RSOA backward propagating ASE photon rate at signal wavelength 1537.7 nm and bias current = 80 mA & optical input power = - 10 dBm

Chapter 4

Arrayed Waveguide Grating

4.1 Introduction

An Integrated-Optic $N \times N$ wavelength multiplexer based on an arrayed-waveguide grating is the key device in wavelength division multiplexing (WDM) optical systems [21]. The multiplexer is composed of an arrayed-waveguide grating, input-output (I-O) waveguides, and focusing slab waveguides. The arrayed-waveguide grating consists of regularly arranged waveguides that join the two slabs and the lengths of adjacent waveguides differ by a constant value. The length difference results in the wavelength-dependent wavefront tilting so light convergence in the output slab is frequency dependent; the arrayed-waveguide operates like a diffraction grating. The point is that the arrayed-waveguide grating operates at high diffraction orders, which leads to wavelength resolutions of better than a nanometer despite its small overall size (of the

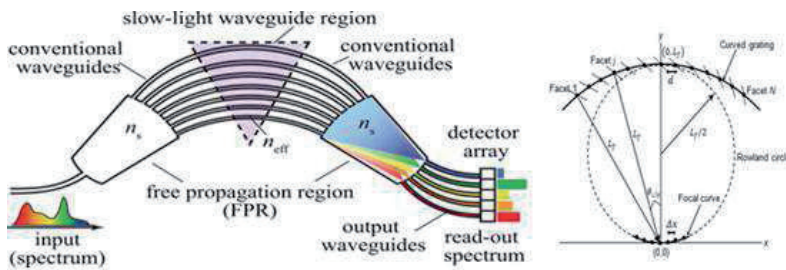


Fig. 4.1. Schematic layout of Arrayed Waveguide Grating

order of centimeters). In addition, the multiplexer has another interesting point. Since the arrayed waveguide is a transmission-type grating, both plural input and plural output waveguides are supported. It is well known that this offers wavelength-selective $N \times N$ connection.

4.2 Waveguide Layout and Basic Equations

Fig 4.1 shows a schematic waveguide layout of the multiplexer. It consists of N input waveguides, N output waveguides, two focusing slab waveguides, and an arrayed waveguide grating, all of which are integrated on the same substrate. The locations of the I-O waveguide ends and arrayed waveguide ends are based on the Rowland circle construction as is used for concave reflection grating mono-chromators. Each arrayed waveguide aperture faces the end of the center I-O waveguide and is widened to reduce slab-channel coupling loss. The array has a sufficient number of waveguides so that all the light power diffracted in the slab can be collected. This means that the arrayed waveguide has a numerical aperture (NA) larger than the 1-0 waveguide, and that the diffracted light in the output slab converges to the same spot size as the input waveguide. That is, the combination of the arrayed waveguide and the two slab waveguides constructs a 1:1 image-formation system [21][22].

The arrayed-waveguide grating consists of regularly arranged waveguides that connect the two slabs. The lengths of adjacent waveguides differ by a constant value ΔL . This structure produces a wavelength-dependent phase shift and the arrayed-waveguide operates like a concave diffraction grating. From the phase match condition, the grating equation is given by [22]:

$$n_s d \sin \theta_i + n_c \Delta L + n_s d \sin \theta_o = m\lambda \quad (4.1)$$

where, $\theta_i = i \cdot \Delta x / L_f$ and $\theta_o = j \cdot \Delta x / L_f$, n_s and n_c are the effective refractive indexes of the slab and channel waveguide, respectively. θ_i and θ_o are the diffraction angles in the input and output slab, respectively. d is the pitch of the arrayed-waveguide grating, m is the diffraction order of the grating, L_f is the focal length of focusing slab waveguide, and λ is the wavelength. i and j are the numbers of the input and output waveguides, respectively. Δx is the spacing of the input and output waveguide along the slab waveguide edge. Here we define the center wavelength as λ_0 which satisfies

$$n_c \Delta L = m\lambda_0 \quad (4.2)$$

This is the pass wavelength for the route $(i,j) = (0,0)$, from the center input waveguide to the center output waveguide.

Angular dispersion, which is the relation between the diffraction angle and frequency f , is obtained by differentiating (4.1), with input at central port, i.e., $\theta_i = 0$.

In the vicinity of $\theta_i = \theta_o = 0$ the result is

$$\frac{d\theta}{df} = -\frac{m\lambda^2}{n_s dc} \frac{n_g}{n_c} \quad (4.3)$$

$$n_g = n_c - \lambda \frac{dn_c}{d\lambda} \quad (4.4)$$

where c is the light velocity in a vacuum, n_g is regarded as the group refractive index of the channel waveguide.

The frequency channel spacing of the multiplexer is given by

$$\Delta f = \frac{\Delta x}{L_f} \left(\frac{d\theta}{df} \right)^{-1} = \frac{\Delta x}{L_f} \left(\frac{m\lambda^2}{n_s dc} \frac{n_g}{n_c} \right)^{-1} [Hz] \quad (4.5)$$

The pass frequency relations for the 16×16 connection are summarized in Table 4.1. Here, the frequency spacing $f_i - f_{i+1}$ is Δf which is given by (4.5). If the frequencies are not periodically assigned, 31 frequencies are needed for 16×16 interconnection that is the number of frequencies is given by $2N - 1$.

4.3 Periodic Assignment of Wavelengths/Frequencies

The periodic assignment of wavelengths/frequencies is a very important property of AWG. Each route has periodic pass frequencies, the spacing of which is referred to as the *Free Spectral Range (FSR)*. If $FSR = N\Delta f$, we can attain an $N \times N$ connection with N frequencies. For example, Table 4.1 shows that f_{-14} is the pass frequency for route $(7,7)$, but $f_{-14} + FSR$ is also a pass frequency for $(7,7)$. Therefore, f_2 can be assigned instead of f_{-14} .

The FSR of the AWG has to be carefully designed to almost match $N\Delta f$. For the order of $m+1$, (4.1) is modified to

$$(n_s + \Delta n_s) d \sin \theta_i + (n_c + \Delta n_c) \Delta L + (n_s + \Delta n_s) d \sin \theta_o = (m+1) \frac{c}{f + FSR} \quad (4.6)$$

where $n_s + \Delta n_s$ and $n_c + \Delta n_c$ are the effective refractive indexes of the slab and channel waveguides, respectively, at the frequency of $f + FSR$. The index change is given by

$$\Delta n_c = \frac{dn_c}{df} FSR = -\frac{c}{f^2} \frac{dn_c}{d\lambda} FSR \quad (4.7a)$$

$$\Delta n_s = \frac{dn_s}{df} FSR = -\frac{c}{f^2} \frac{dn_s}{d\lambda} FSR \quad (4.7b)$$

Finally, from equations (4.1), (4.6) and (4.7), with some approximations, a simplified expression for FSR is given by,

$$FSR = \frac{c}{n_s (\Delta L + d \sin \theta_i + d \sin \theta_o)} \quad (4.8)$$

Table 4.1: Frequency assignment of the Arrayed Waveguide Grating (AWG)

Column: input; Row: output

	-8	-7	...	-1	0	1	...	7	8
-8	f_0	f_{-1}	...	f_{-7}	f_8	f_7	...	f_2	f_1
-7	f_{-1}	f	...	f_8	f_7	f_6	...	f_1	f_0
...
-1	f_{-7}	f_8	...	f_2	f_1	f_0	...	f_{-5}	f_6
0	f_8	f_7	...	f_1	f_0	f_{-1}	...	f_{-6}	f_7
1	f_7	f_6	...	f_0	f_{-1}	f_{-2}	...	f_7	f_8
...
7	f_2	f_1	...	f_{-5}	f_6	f_{-7}	...	f_4	f_3
8	f_1	f_0	...	f_{-6}	f_{-7}	f_{-8}	...	f_3	f_2

4.4 Calculation of Signal Power at Output Ports of AWG

Salz derived an expression for the power spectral density (PSD) of a laser, wherein the laser frequency noise was modeled as a white Gaussian process with a two-sided

spectral density N_0 , leading to a Lorentzian power spectrum with a spectral width (linewidth) $B_L = 2\pi N_0$. Accordingly, the PSD of the Lorentzian laser emission $S_i(f)$ with a center frequency f_{0i} corresponding to the wavelength channel at the i th port is expressed [23] as

$$S_i(f) = \frac{A^2}{4\pi^2 N_0} \left[\frac{1}{1 + \left(\frac{f + f_{0i}}{\pi N_0} \right)^2} + \frac{1}{1 + \left(\frac{f - f_{0i}}{\pi N_0} \right)^2} \right] \quad (4.9)$$

In [24], the authors approximated the modal field for the waveguide array to a Gaussian beam, which determines the far-field intensity pattern of the routed signal spectrum along the image plane. Henceforth, i denotes the index that represents the differential position of an output port with respect to the central port (where $i = 0$). Thus the signal power at the i^{th} output port is a function of angular position θ and is given by

$$P_0^i(\theta) = P_0 e^{-2\theta^2/\theta_w^2} \quad (4.10)$$

where P_0 is the peak optical power in the emission spectrum at the central port, θ is the angular deviation of the i^{th} port from the central port, and θ_w is the 3 dB angular beam width of the Gaussian field. θ_w is related to the other parameters as given by [24], where $\theta_w = (\lambda_c / N_{FPR}) (1 / w_e \sqrt{2\pi})$. Thus θ_w is inversely proportional to the modal field width w_e of the input waveguide. For this reason, single-mode fibers (with low values of w_e) are preferred for both the array and the input/output ports. The combined signal power distribution for a given angle θ_i and frequency f_{0i} given by

$$P_{\text{sig}}^i(\theta, f) = e^{-2\theta^2/\theta_w^2} \left\{ \frac{A^2}{4\pi^2 N_0} \left[\frac{1}{1 + \left(\frac{f + f_{0i}}{\pi N_0} \right)^2} + \frac{1}{1 + \left(\frac{f - f_{0i}}{\pi N_0} \right)^2} \right] \right\} \quad (4.11)$$

Using spectral to spatial mapping relation as follows,

$$(f - f_0) = \frac{L_f \theta}{D} \quad (4.12)$$

Moreover, the center frequency f_{0i} of the i^{th} channel can be expressed in terms of its frequency deviation from the central channel's center frequency f_0 as

$$f_{0i} = f_0 + i\Delta f_{ch} \quad (4.13)$$

Using Eq. (4.12), the above relation between f_{0i} and Δf_{ch} can be transformed into its corresponding angular relation, given by $\theta_{0i} = \theta_0 + i\Delta\theta_{ch} = i\Delta\theta_{ch}$ (assuming $\theta_0 = 0$ without loss of generality). This relation can be used to transform the frequency difference term $(f - f_{0i})$ of Eq. (4.11) into the equivalent angular term. Substituting $f = f_{0i}$, the difference frequency term in Eq. (4.11) can be expressed as [25]

$$f - f_{0i} = \frac{L_f \theta}{D} - i \frac{L_f \Delta\theta_{ch}}{D} \quad (4.14)$$

where, f_0 is the center frequency of the central port, f_{0i} is the center frequency of the i^{th} port ($i \neq 0$), $i\Delta\theta_{ch}$ is the angular separation of the i^{th} port from the central port, Δf_{ch} is the output channel spacing in the frequency domain, and $\Delta\theta_{ch}$ is the output channel spacing in the spatial/angular.

Considering only the positive frequencies of the laser emission spectrum, we get the output PSD for the lightwave at the i^{th} port in terms of the spatial variable as follows [25]:

$$P_{sig}^i(\theta) = \frac{A^2}{\pi B_L} e^{-2(i\Delta\theta_{ch})^2/\theta_w^2} \left[\frac{1}{\left\{ 1 + \left(\frac{2L_f \theta}{B_L D} - i \frac{2L_f \Delta\theta_{ch}}{B_L D} \right)^2 \right\}} \right] \quad (4.15)$$

The total amount of desired signal power captured at the i^{th} port can be obtained by integrating Eq. (4.15) over the angular width $\Delta\theta_{wg}$ ($\Delta\theta_{wg}$ being $< \Delta\theta_{ch}$) of the output

port. On applying the limits of integration, viz. from $i\Delta\theta_{ch} - \Delta\theta_{wg}/2$ to $i\Delta\theta_{ch} + \Delta\theta_{wg}/2$, the signal power at the i^{th} port can be expressed as

$$P_{\text{sig}}^i = \frac{A^2}{\pi} e^{-2(i\Delta\theta_{ch})^2/\theta_w^2} \tan^{-1} \left(\frac{L_f \Delta\theta_{wg}}{B_L D} \right) \quad (4.16)$$

4.5 Calculation of Inter-channel Crosstalk at Output Ports

The analytical expression inter-channel crosstalk power at the i^{th} port can be obtained as the sum of signal power spilled from adjacent ports $P_{i+1}(\theta)$ and $P_{i-1}(\theta)$ over the desired port dimensions, i.e., $(i\Delta\theta_{ch} \pm \Delta\theta_{wg}/2)$. Thus, PSDs of i^{th} and $(i+1)^{\text{th}}$ ports' are integrated over the limits of i^{th} port, as follows [25]:

$$\begin{aligned} P_{xt}^i = & \int_{i\Delta\theta_{ch} - \Delta\theta_{wg}/2}^{i\Delta\theta_{ch} + \Delta\theta_{wg}/2} \frac{A^2}{\pi B_L} \left(e^{-2(\bar{i}\Delta\theta_{ch})^2/\theta_w^2} \right) \times \left[\frac{1}{1 + \left(\frac{2L_f \theta}{B_L D} - (i+1) \frac{2L_f \Delta\theta_{ch}}{B_L D} \right)} \right] d\theta \\ & - \int_{i\Delta\theta_{ch} + \Delta\theta_{wg}/2}^{i\Delta\theta_{ch} - \Delta\theta_{wg}/2} \frac{A^2}{\pi B_L} \left(e^{-2(\bar{i}\Delta\theta_{ch})^2/\theta_w^2} \right) \times \left[\frac{1}{1 + \left(\frac{2L_f \theta}{B_L D} - (i-1) \frac{2L_f \Delta\theta_{ch}}{B_L D} \right)} \right] d\theta \end{aligned} \quad (4.17)$$

And after evaluating the integral, the closed form expression obtained as follows:

$$\begin{aligned} P_{xt}^i = & \frac{A^2}{2\pi} e^{-2(\bar{i}\Delta\theta_{ch})^2/\theta_w^2} \left[\tan^{-1} \left\{ \frac{2L_f}{B_L D} \left(\Delta\theta_{ch} + \frac{\Delta\theta_{wg}}{2} \right) \right\} \right. \\ & \left. - \tan^{-1} \left\{ \frac{2L_f}{B_L D} \left(\Delta\theta_{ch} - \frac{\Delta\theta_{wg}}{2} \right) \right\} \right] \\ & + \frac{A^2}{2\pi} e^{-2(\bar{i}\Delta\theta_{ch})^2/\theta_w^2} \left[\tan^{-1} \left\{ \frac{2L_f}{B_L D} \left(\Delta\theta_{ch} - \frac{\Delta\theta_{wg}}{2} \right) \right\} \right. \\ & \left. - \tan^{-1} \left\{ \frac{2L_f}{B_L D} \left(\Delta\theta_{ch} + \frac{\Delta\theta_{wg}}{2} \right) \right\} \right] \end{aligned} \quad (4.18)$$

For the central port ($i = 0$), this reduces to

$$P_{xt}^0 = \frac{A^2}{\pi} e^{-2\Delta\theta_{ch}^2/\theta_w^2} \left[\tan^{-1} \left\{ \frac{2L_f}{B_L D} \left(\Delta\theta_{ch} + \frac{\Delta\theta_{wg}}{2} \right) \right\} - \tan^{-1} \left\{ \frac{2L_f}{B_L D} \left(\Delta\theta_{ch} - \frac{\Delta\theta_{wg}}{2} \right) \right\} \right] \quad (4.19)$$

This relation shows that device parameters D and L_f determine the focusing ability.

4.6 Results and Discussions

Fig. 4.2 and 4.3, show the output power profile at all the ports of a 16 channel AWG, when input channel powers are +3 dBm and -6 dBm, respectively. Fig. 4.4 and Fig. 4.5, show the loss characteristics of a 16 channel AWG, when input powers are +3 dBm and -6 dBm, respectively. Finally, Fig. 4.6 and 4.7 show the inter-channel crosstalk at different ports of AWG, when the input powers are +3 dBm and -6 dBm, respectively.

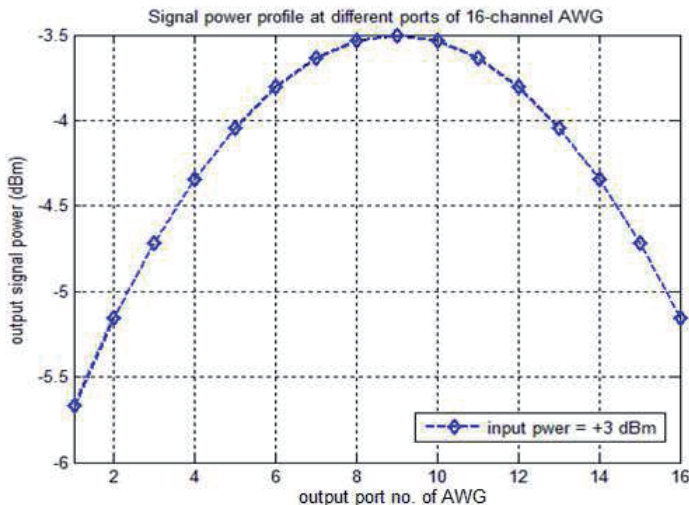


Fig. 4.2. AWG power profile at all the output ports for input power +3 dBm

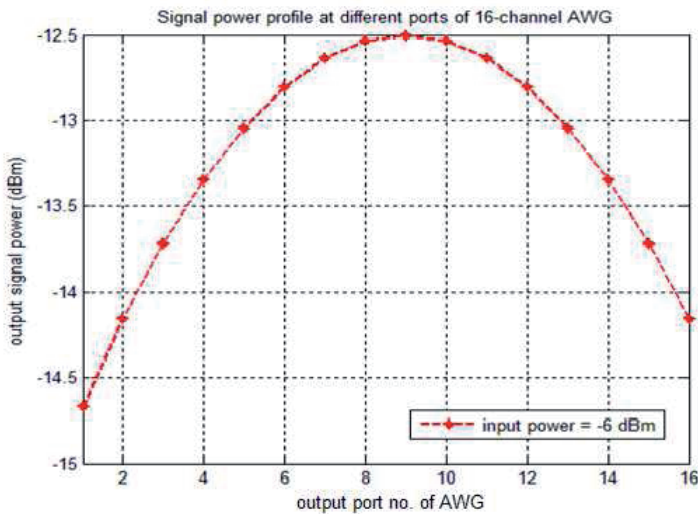


Fig. 4.3. AWG power profile at all the output ports for input power -6 dBm

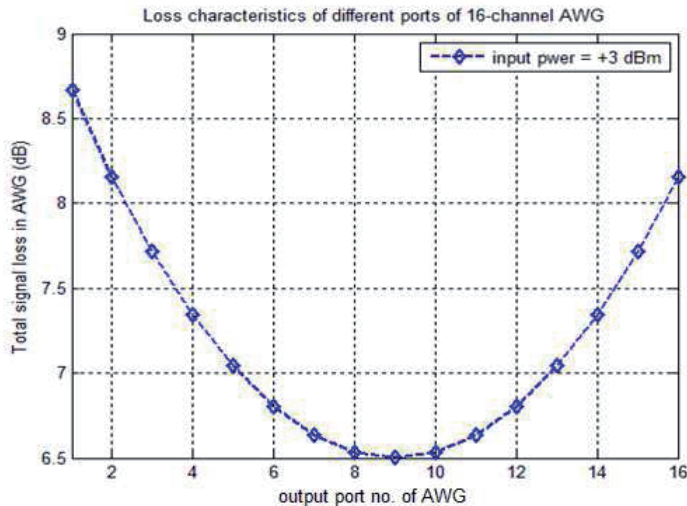


Fig. 4.4. AWG Loss characteristics at all the output ports for input power = +3 dBm

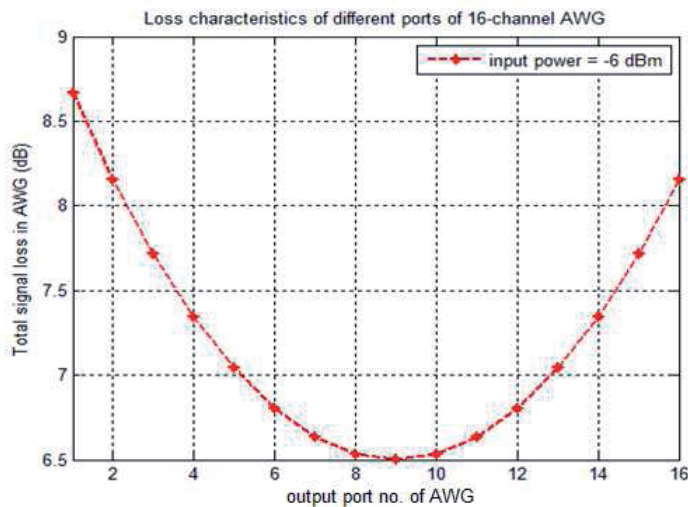


Fig. 4.5. AWG Loss characteristics at all the output ports for input power = -6 dBm

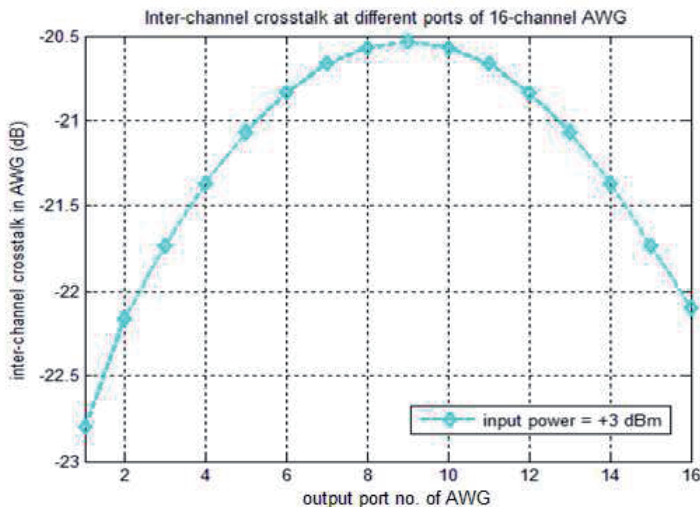


Fig. 4.6. AWG inter-channel crosstalk at input power = +3 dBm

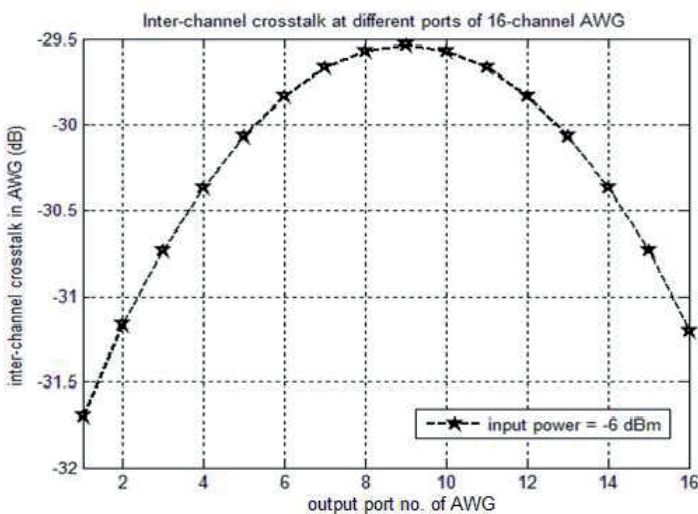


Fig. 4.7. AWG inter-channel crosstalk at input power = -6 dBm

Chapter 5

Erbium Doped Fiber Amplifier

5.1 Introduction

In traditional optical communication systems, optoelectronic regenerators are used between terminals to convert signals from the optical to the electrical domain and then back to the optical domain. Since its first report in 1987, the erbium-doped fiber amplifier (EDFA) has revolutionized optical communications. Unlike optoelectronic regenerators, this optical amplifier does not need high-speed electronic circuitry and is transparent to data rate and format, which dramatically reduces cost. EDFA also provide high gain, high power, and low noise figure. More importantly, all the optical signal channels can be amplified simultaneously within the EDFA in a single optical fiber, thus enabling wavelength division multiplexing (WDM) technology [27].

5.2 The Fundamentals of EDFA

Erbium-doped fiber can be fabricated by several technologies and several analytical models have been proposed in [26][28][32]. Figure 5.1 shows the energy levels of the erbium ion and the associated spontaneous lifetime in the fiber glass host. Erbium-doped fiber is usually pumped by semiconductor lasers at 980 nm or 1480 nm. A three-level model can be used for 980-nm pumps, while a two-level model usually suffices for 1480 nm pumps [27]. Complete inversion can be achieved with 980 nm pumping but not with 1480 nm pumping. The quantum efficiency is higher with 1480 nm pumps. The spontaneous lifetime of the metastable energy level (${}^4I_{13/2}$) is about 10 ms, which is much slower than the signal bit rates of practical interest. As a result of the slow dynamics, inter-symbol distortion and inter-channel crosstalk are negligible — a key advantage of EDFAs.

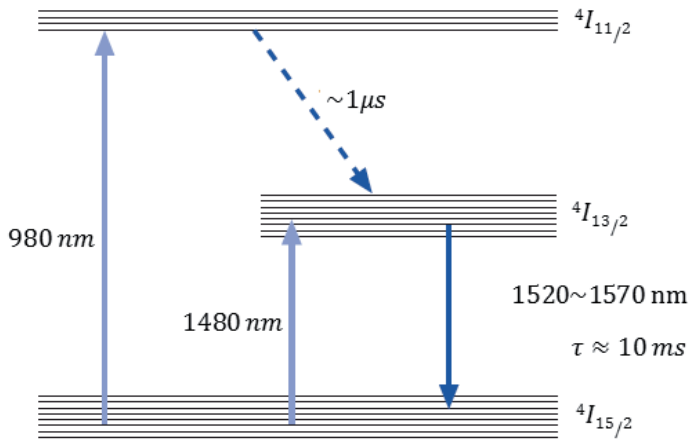


Fig. 5.1. Erbium ion energy level diagram and corresponding spontaneous lifetime[27]

Fig. 5.2 shows the gain and loss coefficient spectra at different inversion levels for erbium-doped fiber co-doped with aluminum and germanium. Under a homogeneous broadening approximation, the overall gain spectrum of any piece of erbium-doped fiber always matches one of the curves after scaling and does not depend on the details of pump power, signal power, and saturation level along the fiber. The gain spectrum is very important for amplifier design.

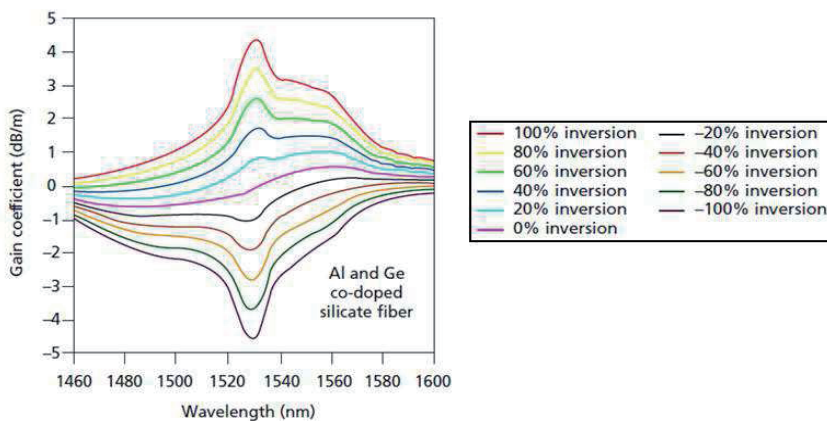


Fig. 5.2. Gain/loss spectra at different inversion levels for an erbium-doped fiber [27]

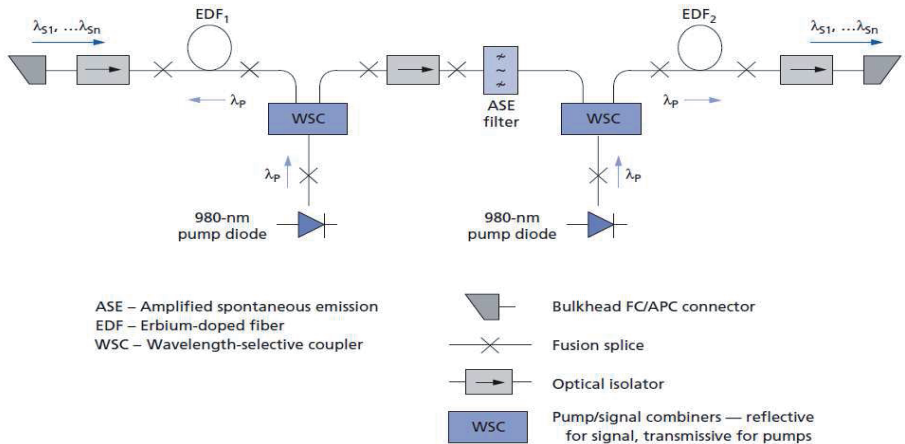


Fig. 5.3. Schematic diagram of a two-stage erbium-doped fiber amplifier for low noise figure and high output power operation [27]

A high inversion level provides low noise figure, while a low inversion level yields high efficiency in the conversion of photons from pump to signal. To achieve both low noise figure and high efficiency, two or more gain stages are generally used — the input stage is kept at a high inversion level and the output stage is kept at a low inversion level. Figure 5.3 shows one such example, in which an amplified spontaneous emission (ASE) filter is inserted in the middle stage to prevent gain saturation caused by the ASE peak around 1530 nm. For optical amplifiers with two or more gain stages, the overall noise figure is mainly decided by the high-gain input stage, and the output power is basically determined by the strongly saturated output stage. The passive components have minimal impact on noise figure and output power when they are in the middle stage.

5.3 Three Level Amplification System

The simplest treatment of the erbium-doped fibre amplifier starts out by considering a pure three-level atomic system. Most of the important characteristics of the amplifier can be obtained from this simple model and its underlying assumptions.

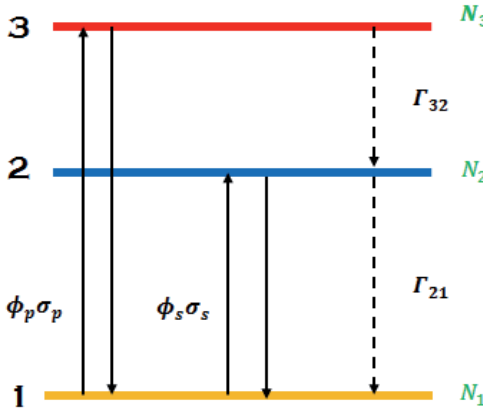


Fig. 5.4. A typical three-level system used for amplifier model **Error! Reference source not found.**

The transition rates between levels 1 and 3 are proportional to the populations in those levels and to the product of the pump flux ϕ_p and pump cross section σ_p . The transition rates between levels 1 and 2 are proportional to the populations in those levels and to the product of the pump flux ϕ_s and pump cross section σ_s . The populations of the levels are labeled as N_1 , N_2 , and N_3 . In particular, we write Γ_{32} as the transition probability from level 3 to level 2 and Γ_{21} as the transition probability from level 2 to level 1.

The rate equations for the population changes are written as [26],

$$\frac{dN_3}{dt} = -\Gamma_{32}N_3 + (N_1 - N_3)\phi_p\sigma_p \quad (5.1)$$

$$\frac{dN_2}{dt} = -\Gamma_{21}N_2 + \Gamma_{32}N_3 - (N_2 - N_1)\phi_s\sigma_s \quad (5.2)$$

$$\frac{dN_1}{dt} = \Gamma_{21}N_2 - (N_1 - N_3)\phi_p\sigma_p + (N_2 - N_1)\phi_s\sigma_s \quad (5.3)$$

In a steady-state situation, the time derivatives will all be zero,

$$\frac{dN_1}{dt} = \frac{dN_2}{dt} = \frac{dN_3}{dt} = 0 \quad (5.4)$$

and the total population is given by

$$N = N_1 + N_2 + N_3 \quad (5.5)$$

From the above equations, we obtain

$$N_3 = \frac{1}{1 + \Gamma_{32} / \phi_p \sigma_p} N_1 \quad (5.6)$$

$$N_2 = \frac{(\phi_p \sigma_p / \Gamma_{32}) + \phi_s \sigma_s}{\Gamma_{21} + \phi_s \sigma_s} N_1 \quad (5.7)$$

Now, by using equation (5.5), we get

$$N_2 - N_1 = \frac{\phi_p \sigma_p - \Gamma_{21}}{\Gamma_{21} + 2\phi_s \sigma_s + \phi_p \sigma_p} N \quad (5.8)$$

The condition for population inversion, and thus for gain on the 2 to 1 is $N_2 \geq N_1$.

The threshold corresponds to $N_2 = N_1$ and results in the following expression for the pump flux required:

$$\phi_{th} = \frac{\Gamma_{21}}{\sigma_p} \quad (5.9)$$

The pump intensity, in units of energy per unit area per unit time, is expressed as $I_p = h\nu_p \phi_p$. The threshold pump intensity is then given very simply by the expression:

$$I_{th} = \frac{h\nu_p \Gamma_{21}}{\sigma_p} \quad (5.10)$$

The equation for signal intensity growth or decay is written as:

$$\frac{dI_s}{dz} = \frac{\frac{\sigma_p I_p}{h\nu_p} - \Gamma_{21}}{\Gamma_{21} + 2\frac{\sigma_s I_s}{h\nu_s} + \frac{\sigma_p I_p}{h\nu_p}} \sigma_s I_s N \quad (5.11)$$

The equation for attenuation of the pump intensity can be written as:

$$\frac{dI_p}{dz} = -\frac{\Gamma_{21} + \frac{\sigma_s I_s}{hv_s}}{\Gamma_{21} + 2\frac{\sigma_s I_s}{hv_s} + \frac{\sigma_p I_p}{hv_p}} \sigma_p I_p N \quad (5.12)$$

5.4 Three level to Two level reduced amplification system

We assume that pumping level 3 belongs to a multiplet different than that of level 2, and that there is rapid relaxation from level 3 to level 2. For all practical purposes, the population in level 3 is effectively zero in steady state and rate equation involves only two levels 1 and 2, with level 3 being involved only via the value of the pump absorption cross section from level 1 to 3. Examples of pump wavelengths in this case are 980 nm, 800 nm, 650 nm, and 540 nm.

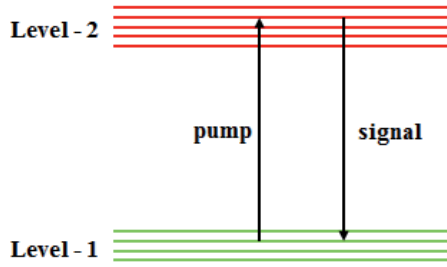


Fig. 5.5. Energy levels of a two-multiplet system, where state 3 is a higher lying state of multiplet 2

Having reduced the three-level system to an effective two-level system, we can write the rate equations so as to involve only the total population densities of multiplets 1 and 2 [26].

$$\frac{dN_2}{dt} = -\Gamma_{21}N_2 + (N_1\sigma_s^{(a)} - N_2\sigma_s^{(e)})\phi_s - (N_2\sigma_p^{(e)} - N_1\sigma_p^{(a)})\phi_p \quad (5.13)$$

$$\frac{dN_1}{dt} = \Gamma_{21}N_2 (N_1\sigma_s^{(a)} - N_2\sigma_s^{(e)})\phi_s + (N_2\sigma_p^{(e)} - N_1\sigma_p^{(a)})\phi_p \quad (5.14)$$

where $\sigma_s^{(a)}$, $\sigma_s^{(e)}$, $\sigma_p^{(a)}$, and $\sigma_p^{(e)}$ represent the signal and pump absorption and emission cross sections, respectively. The total population density N is given by

$$N = N_1 + N_2 \quad (5.15)$$

and we have

$$\frac{dN_1}{dt} = -\frac{dN_2}{dt} = 0 \quad (5.16)$$

Now, we find from equation (5.13) & (5.14), for the case of one pump field and one signal field, that the population density $N_2(z)$, as a function of position z along the fibre, is given by [26],

$$N_2(z) = \frac{\frac{\sigma_s^{(a)}}{h\nu_s} I_s(z, \nu_s) + \frac{\sigma_A^{(a)}}{h\nu_A} I_A(z, \nu_A) + \frac{\sigma_p^{(a)}}{h\nu_p} I_p(z, \nu_p)}{\frac{(\sigma_s^{(a)} + \sigma_s^{(e)})}{h\nu_s} I_s(z, \nu_s) + \frac{(\sigma_A^{(a)} + \sigma_A^{(e)})}{h\nu_A} I_A(z, \nu_A) + \frac{(\sigma_p^{(a)} + \sigma_A^{(e)})}{h\nu_p} I_p(z, \nu_p) + \frac{1}{\tau}} N \quad (5.17)$$

where, I_s is signal intensity, I_A is ASE intensity, I_p is pump intensity and τ is meta-stable carrier lifetime. In general, we will assume that N is independent of z .

The propagation equations for pump power on i^{th} wavelength $P_{p,i}^+$ and signal power on k^{th} wavelength $P_{s,k}^+$, are then written as [30][31],

$$\frac{dP_{p,i}^+(z)}{dz} = (N_2(z)\sigma_{p,i}^{(e)} - N_1(z)\sigma_{p,i}^{(a)})\Gamma_p P_{p,i}^+(z) \quad (5.18)$$

$$\frac{dP_{s,k}^+(z)}{dz} = \left((N_2(z)\sigma_{s,k}^{(e)} - N_1(z)\sigma_{s,k}^{(a)}) \middle/ \left(1 + \frac{P_{\text{tot}}(z)}{P_{\text{sat}}} \right) \right) \Gamma_s P_{s,k}^+(z) \quad (5.19)$$

where $P_{\text{tot}}(z)$ is the total power at length z , and P_{sat} is the saturated output power, i.e., the maximum output power the EDFA can give for any signal input power. An empirical relation that gives the approximate value of absorption cross-section in the region 1550 ± 10 nm [30],

$$\sigma^{(a)}(\lambda) = \frac{4 - 0.1(\lambda - 1540)}{10^{25}} \quad (5.20)$$

The corresponding value of emission cross-section is given by McCumber's relation [31],

$$\sigma^{(e)}(\lambda) = \sigma^{(a)}(\lambda) \exp\left[\frac{hc}{\kappa T} \left(\frac{1}{\lambda_0} - \frac{1}{\lambda}\right)\right] \quad (5.21)$$

The numerical values used for different quantities are given in Table 5.1. The equations above can be generalized to the case of multiple signals and multiple pumps, i.e., for a WDM system. For the N_{ch} number of signals & ASE and N_p pumps, the meta-stable population equation becomes [26][30],

$$N_2(z) = \frac{\sum_{k=1}^{N_{ch}} \frac{\sigma_{s,k}^{(a)}}{h\nu_{s,k}} I_{s,k}(z, \nu_{s,k}) + \sum_{j=1}^{N_{ch}} \frac{\sigma_{A,j}^{(a)}}{h\nu_{A,j}} I_{A,j}(z, \nu_{A,j}) + \sum_{i=1}^{N_p} \frac{\sigma_{p,i}^{(a)}}{h\nu_{p,i}} I_{p,i}(z, \nu_{p,i})}{\sum_{k=1}^{N_{ch}} \frac{(\sigma_{s,k}^{(a)} + \sigma_{s,k}^{(e)})}{h\nu_{s,k}} I_{s,k}(z, \nu_{s,k}) + \sum_{j=1}^{N_{ch}} \frac{(\sigma_{A,j}^{(a)} + \sigma_{A,j}^{(e)})}{h\nu_{A,j}} I_{A,j}(z, \nu_{A,j}) + \sum_{i=1}^{N_p} \frac{(\sigma_{p,i}^{(a)} + \sigma_{p,i}^{(e)})}{h\nu_{p,i}} I_{p,i}(z, \nu_{p,i}) + \frac{1}{\tau}} N \quad (5.22)$$

where,

$$\begin{aligned} I_{s,k}(z, \nu_{s,k}) &= P_{s,k}(z, \nu_{s,k}) \Gamma_s / A_s \\ I_{A,j}(z, \nu_{A,j}) &= P_{A,j}(z, \nu_{A,j}) \Gamma_s / A_s \\ P_{A,j}(z, \nu_{A,j}) &= P_{A,j}^+(z, \nu_{A,j}) + P_{A,j}^-(z, \nu_{A,j}) \\ I_{p,i}(z, \nu_{p,i}) &= P_{p,i}(z, \nu_{p,i}) \Gamma_p / A_p \end{aligned} \quad (5.23)$$

In WDM case, the number of wavelengths is more than 1, but, the total meta-stable population is constant. So, the signal gains on all the channels are lesser than one channel scenario. The gains are also affected by wavelength dependency of the gain characteristics of EDFA. Moreover, if signal powers in some channels are more than others, not only they are supposed to get lesser gain, but, also they make the other weak signals suffer from lesser gain. This phenomenon is called "Capture Effect" in EDFA.

Table 5.1: EDFA geometrical and material parameters used in the steady-state model

Symbol	Parameter	Value
N	Total erbium dopant concentration	$1 \times 10^{25} \text{ m}^{-3}$
N_2	Meta-stable level population density	—
N_1	Ground level population density	—
τ	Meta-stable level carrier lifetime	10 ms
Γ_s	Mode overlap factor for signal @ 1550 nm region	0.8
$\Gamma_{p,980}$	Mode overlap factor for pump @ 980 nm	0.85
$\Gamma_{p,1470}$	Mode overlap factor for pump @ 1470 nm	0.72
A_s	Effective area of cross-section for signal @ 1550 nm region	$52.6 \mu\text{m}^2$
$A_{p,980}$	Effective area of cross-section for pump @ 980 nm	$3.36 \mu\text{m}^2$
$A_{p,1470}$	Effective area of cross-section for pump @ 1470 nm	$4.97 \mu\text{m}^2$
P_{sat}	Saturation output power	15-23 dBm
L_{980}	Total length of fibre for pump @ 980 nm	8.2 m
L_{1470}	Total length of fibre for pump @ 1470 nm	10.6 m
Δz	Length of each small segment of the fibre	0.2 m
Δv	ASE bandwidth for each channel frequency	250 GHz
λ_0	Constant that depends on the details of electronic structures	1526 nm
$\sigma_{p,980}^{(a)}$	Pump absorption cross-section @ 980 nm	$2.58 \times 10^{-25} \text{ m}^2$
$\sigma_{p,980}^{(e)}$	Pump emission cross-section @ 980 nm	≈ 0
$\sigma_{p,1470}^{(a)}$	Pump absorption cross-section @ 1470 nm	$1.64 \times 10^{-25} \text{ m}^2$
$\sigma_{p,1470}^{(e)}$	Pump emission cross-section @ 1470 nm	$6.48 \times 10^{-26} \text{ m}^2$
$\sigma_{s,k}^{(a)}$	Signal & ASE absorption cross-section	—
$\sigma_{s,k}^{(e)}$	Signal & ASE emission cross-section	—
P_{sat}	Saturation output power	20 – 30 dBm

5.5 Amplified Spontaneous Emission

To compute the ASE at the output of the fibre, we need to first calculate the spontaneous emission power at a given point of fibre. This power is sometimes referred

to as an equivalent noise power. For a single transverse mode fibre with two independent polarizations for a given mode at frequency ν , the noise power in a bandwidth $\Delta\nu$ [26], corresponding to spontaneous emission, is equal to

$$P_{ASE}^0 = 2h\nu\Delta\nu \quad (5.24)$$

Although the signal propagates in one direction only, but, ASE is bidirectional. So, ASE has two components, i.e., forward ASE & backward ASE. The propagation equations for the forward ASE power ($P_{A,j}^+$) and backward ASE power ($P_{A,j}^-$) are given by [30][31],

$$\frac{dP_{A,j}^+(z)}{dz} = \frac{\left(N_2(z)\sigma_{A,j}^{(e)} - N_1(z)\sigma_{A,j}^{(a)}\right)}{\left(1 + \frac{P_{tot}(z)}{P_{sat}}\right)} \Gamma_A P_{A,j}^+(z) + 2N_2(z)\sigma_{A,j}^{(e)}\Gamma_A h\nu_{A,j}\Delta\nu \quad (5.25)$$

$$\frac{dP_{A,j}^-(z)}{dz} = -\frac{\left(N_2(z)\sigma_{A,j}^{(e)} - N_1(z)\sigma_{A,j}^{(a)}\right)}{\left(1 + \frac{P_{tot}(z)}{P_{sat}}\right)} \Gamma_A P_{A,j}^-(z) - 2N_2(z)\sigma_{A,j}^{(e)}\Gamma_A h\nu_{A,j}\Delta\nu \quad (5.26)$$

For ASE, the values of emission cross-section ($\sigma_A^{(e)} = \sigma_s^{(e)}$), absorption cross-section ($\sigma_A^{(a)} = \sigma_s^{(a)}$) and mode overlap factors ($\Gamma_A = \Gamma_s$) are same. The second term in the RHS expression has a 2 multiplied because although signal is either TE or TM mode, but, ASE is generated in both modes. $\Delta\nu$ is the ASE bandwidth and is considered 2 nm or 250 GHz.

5.6 Algorithm for Numerical Solution of the Equations

As the EDFA model equations cannot be solved analytically, a numerical solution is required. In the numerical model the amplifier is split into a number of sections labeled from $i = 1$ to N_z , similar to RSOA model in Chapter – 3, i.e., total length L is divided into small segments of length Δz . The signal, pump and spontaneous emission powers are estimated at the section interfaces. The signal & ASE powers can be stored in matrices of dimension ($N_{ch} \times N_z$) and pump powers can be stored in matrix of dimension ($N_p \times N_z$). meta-stable carrier densities are stored in matrix of dimension (1 $\times N_z$).

The steps of the algorithm are described as follows:

Step – 1: Initialize all the signal, pump and spontaneous emission powers inside the amplifier for all segments to zero. The meta-stable carrier density for segment – 1 is determined by using signal, ASE & pump powers falling upon EDFA externally.

Step – 2: The iteration now begins. The coefficients of the traveling-wave equations are computed.

Step – 3: The signal, pump and noise powers are estimated using finite difference solutions of travelling-wave equations for signal, pump and ASE powers. Forward differences are used for positive traveling-waves and backward differences for negative traveling-waves. Based on these values, estimate the meta-stable state carrier density of the next segment.

Step – 4: The iteration continues until the percentage change in the signal, pump & noise powers and carrier density throughout the EDFA between successive iterations is less than the desired tolerance.

When the iteration stops, parameters such as signal gain, pump power and output spontaneous noise power are calculated.

A sample MATLAB code for this model is available in the following link:

<http://www.mathworks.in/matlabcentral/fileexchange/48263-erbium-doped-fiber-amplifier-edfa--model>

5.7 Comparison of simulation results with a real device datasheet ratings

For the EDFA modeling in single wavelength & WDM scenario, the steady-state model proposed by P. C. Becker [26], E. Desurvire [28], C. Berkdemir [31] and P. R. Morkel [32] were closely followed. The technical reports on EDFA by A. K. Srivastava [27], D. Baney [30] were also followed for details of device parameters. The simulation results were found to be very close to real EDFA devices. A comparison between the

simulation results and ratings of a real device from datasheet [35], is given in Table 5.2.

Table 5.2: Comparison between real device ratings & simulation results [35]

Parameter	Test Condition	Datasheet Rating	From simulation	Unit
Wavelength Range	40 mW & 20 °C	1530 – 1565	1530 – 1565	nm
Small Signal Gain	40 mW & 20 °C	35	34.9	dB
Saturated Output Power	40 mW & 20 °C Pin = -20 dBm	20	20	dBm
Integrated ASE Power	40 mW & 20 °C Pin = -50 μW	-22	-21.54	dBm
Pump Power Range	Across temp. range	10 – 100	10 – 100	mW
Optical I/P Power	40 mW & 20 °C	-22 to +6	-22 to +6	dBm
Backward ASE power	40 mW & 20 °C	< 25	-10.5	dBm

5.8 Results and Discussions

Fig. 5.6 shows the gain characteristics of EDFA vs. wavelength for different pump powers, when fiber length = 5m and Fig. 5.7 shows the same when fiber length = 10m. Clearly, from these graphs, inference can be drawn that as the length of fiber is increased, the gain also increases proportionally. Fig. 5.8 shows the in general single-pass gain of EDFA with different lengths when the pump power is varied, where a gain saturation effect is observed for input signals lesser than -25 dBm. In Fig. 5.9, the small-signal gain of EDFA is shown vs. input signal power at signal wavelength = 1550 nm, with a pump power = 40 mW at 980 nm and in Fig. 5.10, the ASE power has been shown with the same configuration. In both these graphs, a saturation effect is observed around a pump power of 0.01 dBm. Fig. 5.11 and 5.12 shows the small-signal gain and ASE power for different pump powers for a signal power 50 μW at wavelength = 1550 nm. Fig. 5.13 to 5.15 shows the distribution of signal power, forward & backward ASE and carrier density distributions along the length of the fiber. Fig. 5.16 shows the WDM

gain on 16 channels in the 1550 nm window and Fig. 5.17 shows the same on 32 channels. Clearly, these two graphs validate the “capture effect” phenomenon, i.e., when number of channels increases, the total gain reduces as well as gain on different wavelength no longer remains uniform.

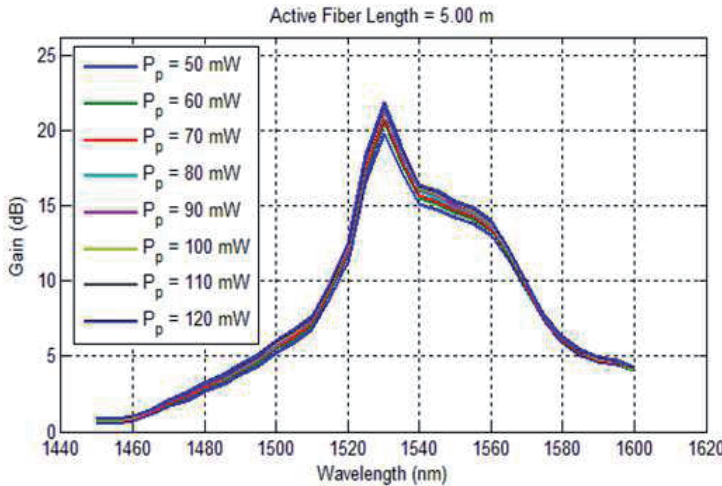


Fig. 5.6. Gain characteristics of EDFA vs. wavelength for fibre length = 5m

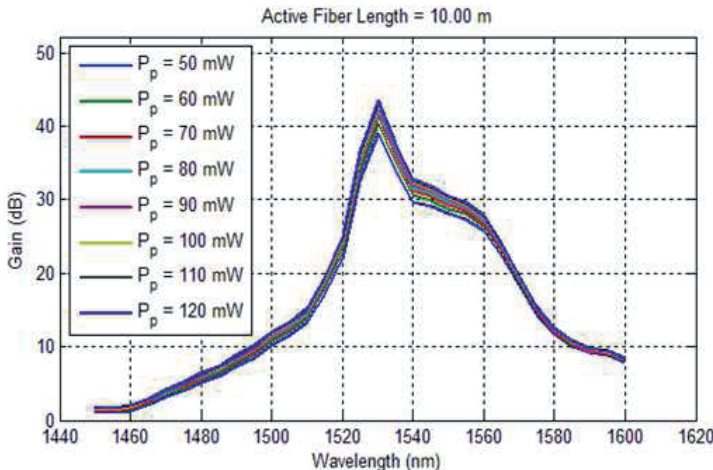


Fig. 5.7. Gain characteristics of EDFA vs. wavelength for fibre length = 10m

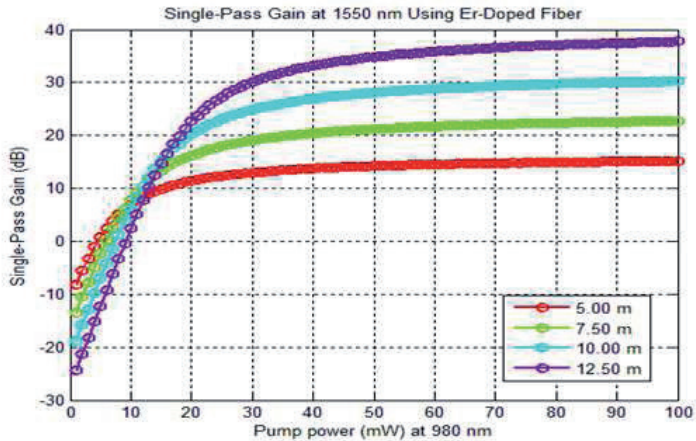


Fig. 5.8. Single-pass gain of EDFA of different lengths vs. pump power at 980 nm

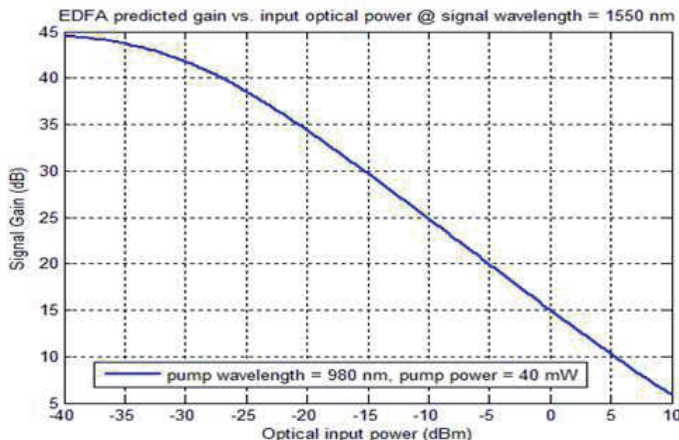


Fig. 5.9. Small-signal gain of EDFA at 1550 nm vs. optical input power at pump = 980 nm, 40 mW

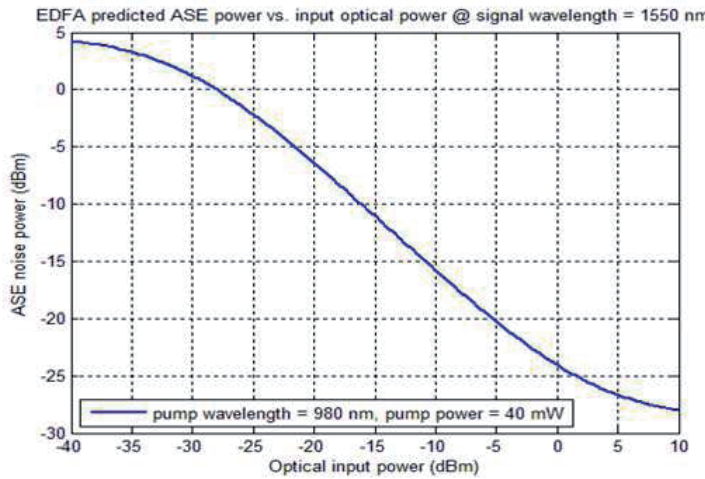


Fig. 5.10. ASE output of EDFA at 1550 nm vs. optical input power at pump = 980 nm, 40 mW

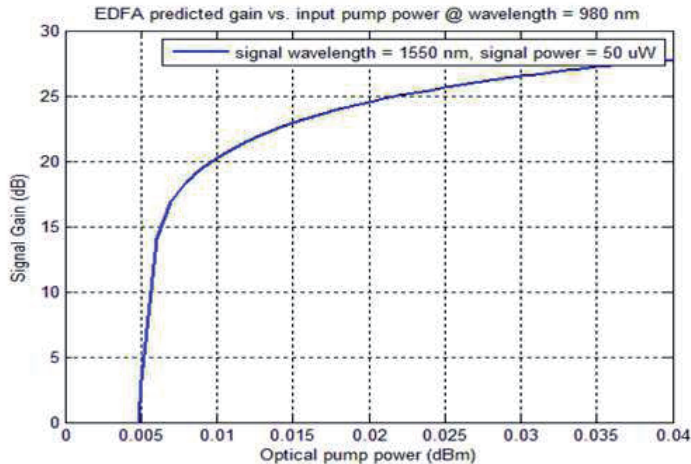


Fig. 5.11. Signal gain of a signal = 1550 nm, 50 μ W vs. pump power at 980 nm

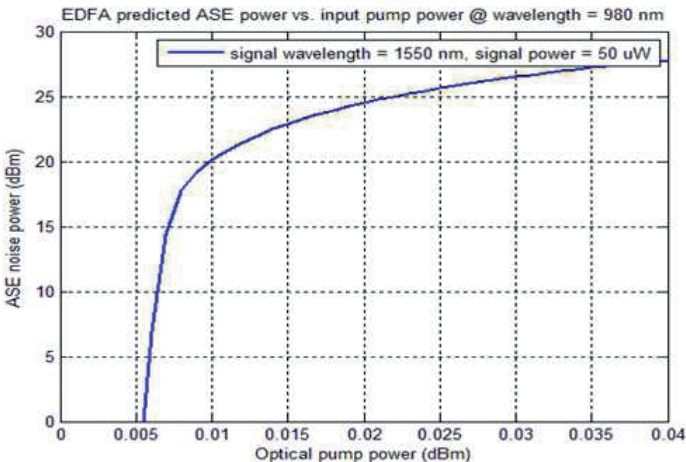


Fig. 5.12. ASE power generated with a signal = 1550 nm, 50 μ W vs. pump power at 980 nm

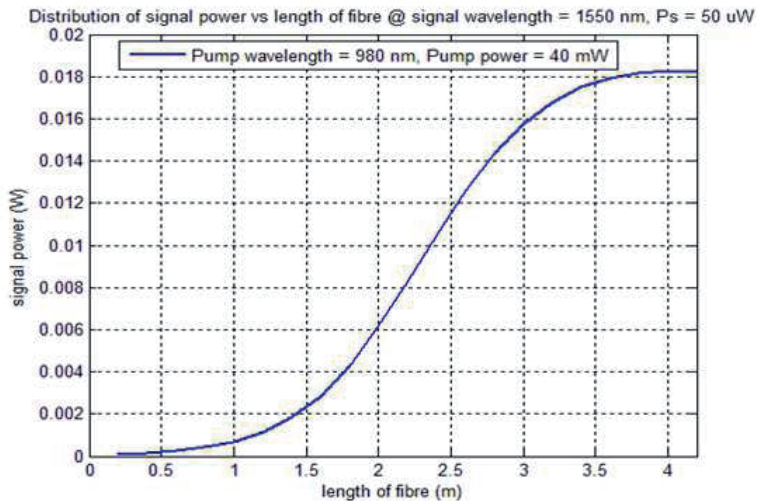


Fig. 5.13. Amplification of a signal = 1550 nm, 50 μ W along the length of fibre

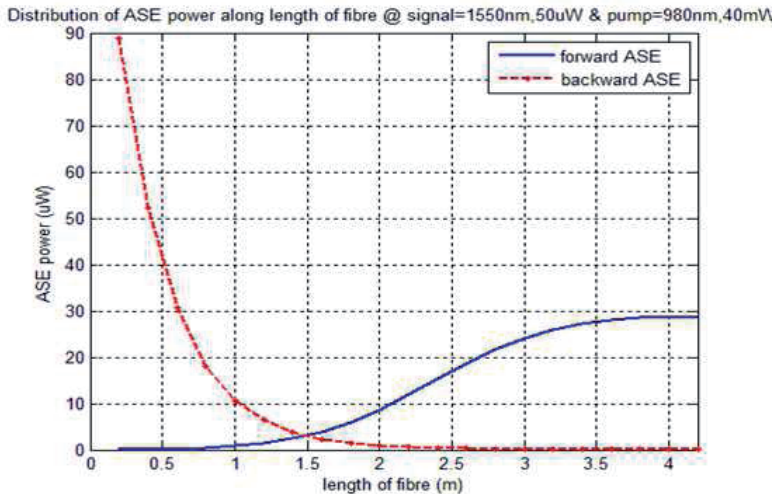


Fig. 5.14. Distribution of Forward & Backward ASE with a signal = 1550 nm, 50 μ W along the length of fibre

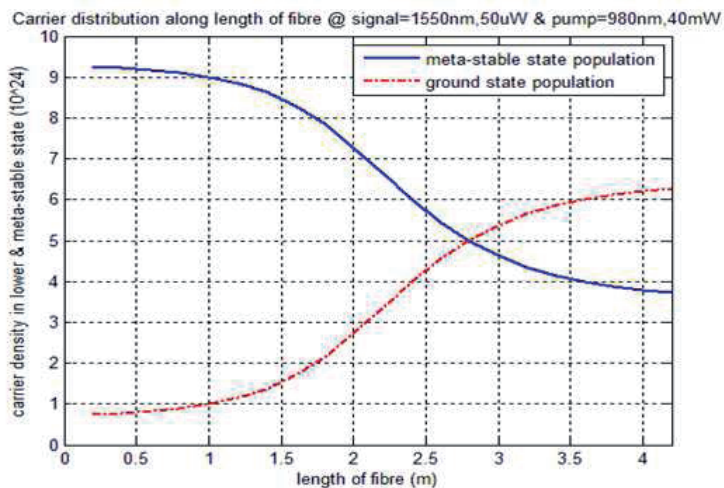


Fig. 5.15. Distribution of Meta-stable & ground carriers with a signal = 1550 nm, 50 μ W along the length of fibre

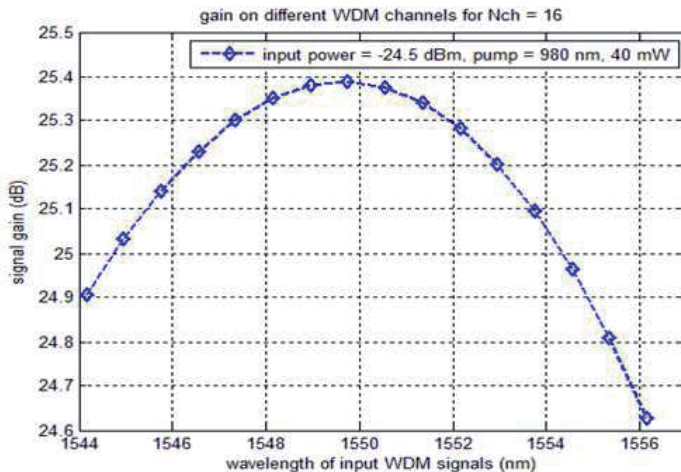


Fig. 5.16. WDM gain on different wavelengths when total no. of channels = 16, signal power = -24.5 dBm, pump = 980 nm, 40 mW

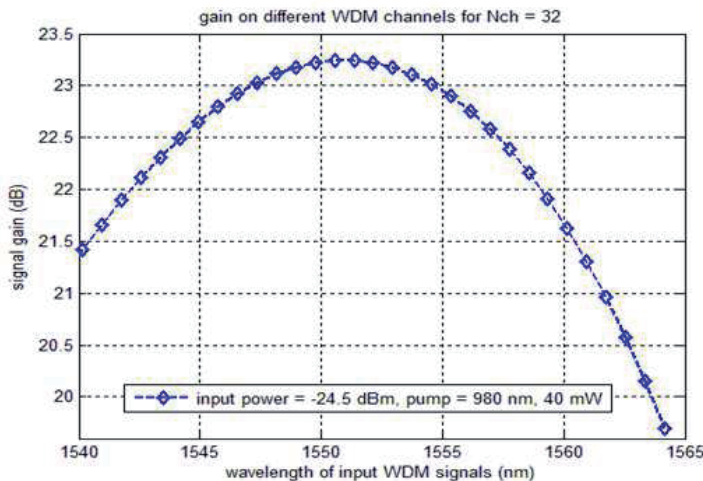


Fig. 5.17. WDM gain on different wavelengths when total no. of channels = 32, signal power = -24.5 dBm, pump = 980 nm, 40 mW

Chapter 6

End-to-End Bit Error Rate (BER) Analysis

6.1 Introduction

The end-to-end bit error rate calculation is the most important thing in the design of uplink with reflective ONUs. Here an intensity-modulated direct-detection (IM-DD) system for optical communication channels for the evaluation of the BER at the receiving end has been considered. Furthermore, we consider crosstalk contribution from only two neighboring channels and the beat noise is assumed to affect only the binary “1” transmissions. The beat noise variance takes into account the probability of occurrence for a binary “1” p_{r_on} . The datarate R_b is considered to be 1 Gbps, which can be extended possibly upto 10 Gbps. For the uplink, when lights from CW lasers are emitted, their linewidth, B_L can be considered from 100 MHz to 1.5 GHz, but when the carriers are modulated at RSOA, the linewidth become the root-mean square average of B_L and $BW (=R_b / 2)$ [25], i.e., $B_{L_new} = \sqrt{\frac{1}{2}(B_L^2 + BW^2)}$.

6.2 Computation of all the noise components in the network

The noise components corresponding to the i^{th} channel are expressed in terms of the constituent noise variance. The thermal noise variance σ_{th}^2 , relative intensity noise variances $\sigma_{rin0}^2 / \sigma_{rin1}^2$, shot noise variances $\sigma_{sh0}^2 / \sigma_{sh1}^2$, signal-ASE beat noise variances $\sigma_{s-ASE0}^2 / \sigma_{s-ASE1}^2$, and ASE-ASE beat noise variances $\sigma_{ASE-ASE0}^2 / \sigma_{ASE-ASE1}^2$, for a “0” bit and a “1” bit [14][33], respectively, are given by

$$\sigma_{th}^2 = \frac{4\kappa T B_e}{R_L} \quad (6.1)$$

$$\sigma_{sh0}^2 = 2qR_\lambda \left(\varepsilon P_{sig}^i + P_{ASE}^i \right) B_e \quad \sigma_{sh1}^2 = 2qR_\lambda \left(P_{sig}^i + P_{ASE}^i \right) B_e \quad (6.2)$$

$$\sigma_{rin0}^2 = \left(\varepsilon R_\lambda P_{sig}^i \right)^2 \langle RIN \rangle B_e \quad \sigma_{rin1}^2 = \left(R_\lambda P_{sig}^i \right)^2 \langle RIN \rangle B_e \quad (6.3)$$

$$\sigma_{s-ASE0}^2 = 4 \left(\varepsilon R_\lambda P_{sig}^i \right) \left(\frac{R_\lambda P_{ASE}^i B_e}{\Delta \nu} \right) \quad \sigma_{s-ASE1}^2 = 4 \left(R_\lambda P_{sig}^i \right) \left(\frac{R_\lambda P_{ASE}^i B_e}{\Delta \nu} \right) \quad (6.4)$$

$$\sigma_{ASE-ASE0}^2 = \left(\frac{R_\lambda P_{ASE}^i}{\Delta \nu} \right)^2 (2\Delta \nu - B_e) B_e \quad \sigma_{ASE-ASE1}^2 = \left(\frac{R_\lambda P_{ASE}^i}{\Delta \nu} \right)^2 (2\Delta \nu - B_e) B_e \quad (6.5)$$

where, the symbols used in the above expressions represent the variables as defined in Table 6.1. Furthermore, inter-channel crosstalk variance, signal-crosstalk beat noise variance, crosstalk-crosstalk beat noise variance can also be incorporated by following similar method as in [25].

Considering all the constituent noise components, the standard deviations of total noise for the reception of “0” and “1” bits (σ_0 and σ_1 , respectively) for every i^{th} channel, are given as,

$$\sigma_0 = \sqrt{\sigma_{th}^2 + \sigma_{sh0}^2 + \sigma_{rin0}^2 + \sigma_{s-ASE0}^2 + \sigma_{ASE-ASE0}^2} \quad (6.6)$$

$$\sigma_1 = \sqrt{\sigma_{th}^2 + \sigma_{sh1}^2 + \sigma_{rin1}^2 + \sigma_{s-ASE1}^2 + \sigma_{ASE-ASE1}^2} \quad (6.7)$$

Accordingly, the decision threshold I_{th} in terms of the noise variance components is computed as,

$$I_{th} = \frac{R_\lambda P_{sig}^i \sigma_0 + \varepsilon R_\lambda P_{sig}^i \sigma_1}{\sigma_0 + \sigma_1} \quad (6.8)$$

6.3 BER calculation with Conventional Receiver

In the network, for the uplink path, as shown in Fig. 2.2 & Fig. 2.3, the power launched from the CW lasers usually lies in the range -6 to +3 dBm. Then the signal passes through different devices and suffers from many losses and amplifications. The loss at every circulator is 0.5 dB, loss at every band splitter/combiner is 0.5 dB, insertion loss of AWG is 6.5 dB and attenuation in the fibre is 0.2 dB/Km. The amplification of different amplifiers e.g., EDFA & RSOA, occurred depending on input signal power level. While passing through amplifiers, amplified spontaneous emission (ASE) noise is also accumulated with the signal, which makes the RSOA

based PON a noise-based network. The PIN photodetector has a receiver sensitivity of -36 to -26 dBm. For the sake of simplicity, the AWG crosstalk has been ignored here, because signal to crosstalk ratio is usually of the order -40 to -30 dB, very much smaller than other dominant noise components, viz, shot noise, ASE noise etc.

Table 6.1: Description of system parameters

Parameter	Description
κ	Boltzmann constant
B_e	noise equivalent bandwidth (= data rate/2)
η_{th}	noise power spectral density
T	absolute temperature in degrees Kelvin
R_L	load resistance
q	electronic charge
ε	laser extinction ratio (= 0.1)
R_λ	photodetector responsivity (= 0.8)
RIN	relative intensity noise coefficient (= -150 dB/Hz)
n_{adj}	number of adjacent ports contributing to crosstalk (= 2)
ξ_{pol}	polarization mismatch factor (= 0.5)
P_{sig}^i	optical signal power of the i^{th} channel
P_{ASE}^i	ASE noise power of the i^{th} channel
$P_{adj\pm 1}^i$	optical signal power from adjacent channel
P_{xt}^i	optical crosstalk power of the i^{th} channel
σ_{th}^2	thermal noise variance
σ_{sh0}^2	shot noise variance for “0” bit
σ_{sh1}^2	shot noise variance for “1” bit
σ_{rin0}^2	laser relative intensity noise variance for “0” bit
σ_{rin1}^2	laser relative intensity noise variance for “1” bit
$\sigma_{sg_xt}^2$	signal–crosstalk beat variance

σ_{xt}^2	crosstalk variance from adjacent channels
$\sigma_{xt_xt}^2$	crosstalk–crosstalk beat variance

Finally, using Gaussian statistics for receiver noise processes for the “0” and “1” receptions (with σ_0 and σ_1 as the respective noise variances), the BER with a conventional receiver [25], is expressed as follows:

$$P_e(\text{conv}) = \frac{1}{4} \left\{ \operatorname{erfc} \left[\frac{R_\lambda P_{\text{sig}}^i - I_{\text{th}}}{\sqrt{2}\sigma_1} \right] + \operatorname{erfc} \left[\frac{I_{\text{th}} - \varepsilon R_\lambda P_{\text{sig}}^i}{\sqrt{2}\sigma_0} \right] \right\} \quad (6.9)$$

Putting the expression for I_{th} in (6.10) we get a more simplified expression as follows:

$$P_e(\text{conv}) = \frac{1}{2} \operatorname{erfc} \left(\frac{R_\lambda (P_{\text{sig}}^i - \varepsilon P_{\text{sig}}^i)}{\sqrt{2}(\sigma_1 + \sigma_0)} \right) \quad (6.10)$$

The consideration of all signal loss and amplification with ASE noise generation for proposed architecture with CW lasers at OLT, as seen in Fig. 2.2, can be represented by the flow-diagram in Fig. 6.1, on the basis of which the final BER calculation is done.

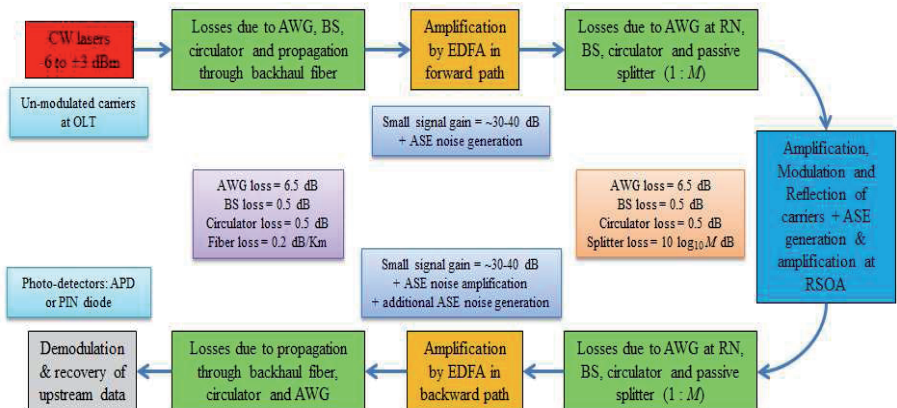


Fig. 6.1. Flow diagram for considering all signal losses & amplification with ASE generation in the upstream for architecture with CW lasers at OLT

Similarly, the consideration of all signal loss and amplification with ASE noise generation for proposed architecture with CW lasers near RN, as seen in Fig. 2.3, can be represented by the flow-diagram in Fig. 6.2, on the basis of which the final BER calculation is done. However, there are a few parameters, based on which BER can vary according to design. The length of forward and backward path EDFA, their pump power, the length of active region of RSOA and it's bias current, are the primary.

6.4 BER calculation with Burst Mode Receiver (BMR)

In Long-Reach PON, the ONUs are usually situated at different distances from the RN. The main feeder fiber may be of 90-100 Km, but, after RN, one ONU may be at 20 Km far, one may be 50 Km far and likewise. This variation of distance causes a serious problem in recovering of data from the upstream. The power levels of signals from ONUs situated far are lesser than that of ONUs situated nearer. This variation of signal powers makes it difficult to determine a proper decision threshold, which leads to more bit error rate and poorer system performance in the upstream [37]. Thus the necessity of design of BMR for high datarate systems was felt and first realized by Ota and Swartz in [38][39]. The Burst Mode Receiver in the OLT dynamically generates the threshold from the received data for each burst of data. Normally the conventional

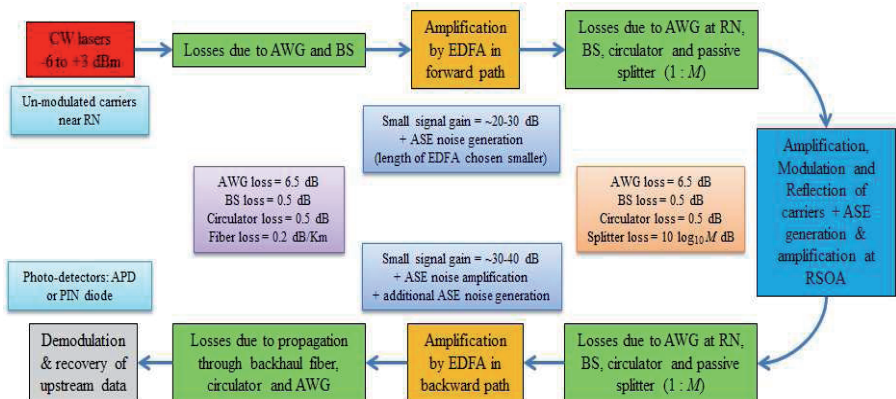


Fig. 6.2. Flow diagram for considering all signal losses & amplification with ASE generation in the upstream for architecture with CW lasers near RN

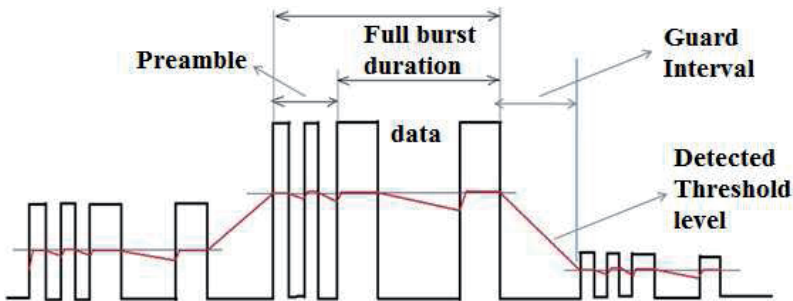


Fig. 6.3. The dynamic threshold variation of a BMR [37]

receivers are ac coupled with automatic gain control. For burst mode data clock recovery and threshold is to be determined in a short time (typically within a small fraction of packet duration). So dc coupling is used in Burst mode receiver. For determining the threshold in Burst mode receiver a few preamble bits are added at the beginning of the packet. The received burst mode data at OLT and its dynamic threshold is shown in Fig. 6.3.

For an optical communication system with conventional receiver, the probability distribution functions (PDF) for '1' and '0', both are Gaussian and the distribution for '1' is flatter than that of '0's. Thus the decision threshold can be very well defined.

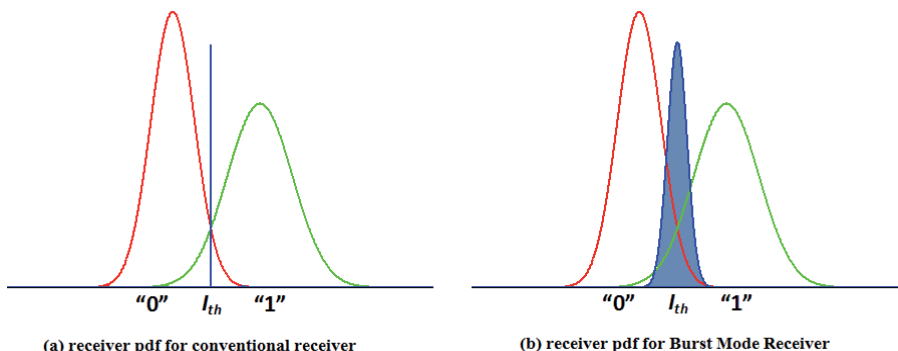


Fig. 6.4. (a) The PDF of symbols at receiver with conventional receiver [34], (b) The PDF of symbols at receiver with Burst Mode Receiver [36]

But, for BMR, the sharp decision boundary is difficult to determine. In this case, the decision boundary also becomes a Gaussian distribution function, as shown in Fig. 6.4.

6.4.1 Structure of Burst Mode Receiver

The structure of typical Burst Mode Receiver [36] is shown in Fig. 6.5. Several similar or better designs have been demonstrated in [37][38][39]. Usually, an ideal BMR consists of a preamplifier and a photodiode, preferably APD or PIN diode. The

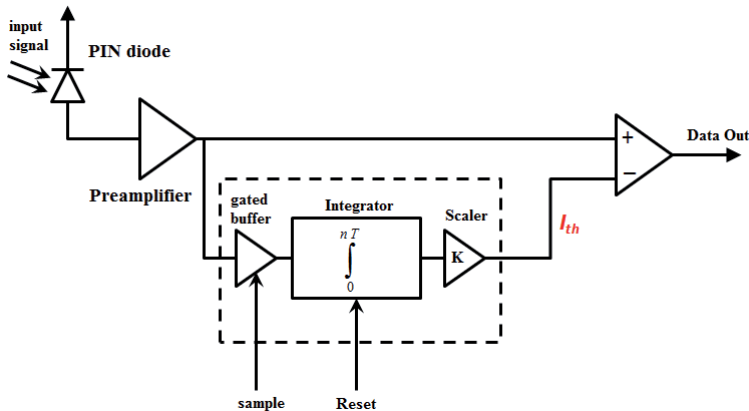


Fig. 6.5. Ideal feed-forward burst mode receiver with an integrating sample and hold for the determination of the proper threshold [36]

signal at the output of photodiode is connected to the positive terminal of the decision circuit. The signal from the photodiode is also fed to a peak detector circuit followed by an integrator (which integrates over the preamble bits) & scaler to determine the threshold. This threshold is connected to the negative terminal of the decision circuit and in the positive terminal the received signal is fed to obtain the data stream.

6.4.2 Analytical BER model for BMR

The BER of BMR is evaluated by averaging the BER of conventional receiver by the PDF of the threshold. The distribution of the threshold due to noise is similar to that of logical “1” and logical “0”. The threshold distribution is Gaussian given by equation 6.17 and the variance decreases as the number of preamble bits, n , increases.

The PDF of the threshold current is given as follows:

$$f(I_t) = \sqrt{\frac{n}{2\pi\sigma_{avg}^2}} \exp\left(-n \frac{(I_t - I_{th})^2}{2\sigma_{avg}^2}\right) \quad (6.11)$$

where, I_t is the photodetector current, I_{th} is the threshold current and σ_{avg} is the average of σ_0 and σ_1 , i.e., $\sigma_{avg} = (\sigma_0 + \sigma_1)/2$.

Thus, averaging the BER of conventional receiver with the PDF in equation 6.17, we get,

$$P_e(burst) = \int_{-\infty}^{\infty} P_e(conv)f(I_t)dI_t \quad (6.12)$$

which can be further expanded as follows:

$$P_e(burst) = \int_{-\infty}^{\infty} \left[\frac{1}{2} \operatorname{erfc} \left(\frac{R_\lambda (P_{sig}^i - \varepsilon P_{sig}^i)}{\sqrt{2}(\sigma_1 + \sigma_0)} \right) \times \sqrt{\frac{n}{2\pi\sigma_{avg}^2}} \exp\left(-n \frac{(I_t - I_{th})^2}{2\sigma_{avg}^2}\right) \right] dI_t \quad (6.13)$$

There is no closed form expression for the integral in equation (6.19) and thus it has to be evaluated numerically.

6.5 Results and Discussions

In this section, from Fig. 6.6 to Fig. 6.9, at first we see the BER at different channels for different reach distances for the architecture with CW laser at OLT, when power transmitted is +3 dBm in all channels, with a conventional receiver. In Fig. 6.10 and Fig. 6.11, we see the BER in all channels with BMR for different number of preamble bits. Clearly as reach distance increases, even with using more number of preamble bits, it becomes difficult to match the performance of a conventional receiver for a BMR. The cyan dashed blue line in these plots indicates the BER with a conventional receiver for the same reach distance. The design parameters, e.g., length of forward and backward EDFA, RSOA active region length and bias current were fixed to some optimized value. If they are changed, the results may differ than the figures.

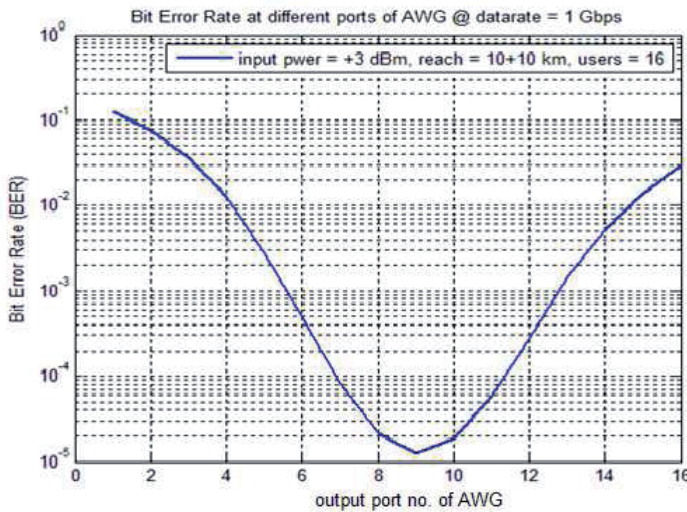


Fig. 6.6. Bit Error Rates on all 16 channels for input power = +3 dBm, reach = 10+10 Km & 16 users at a datarate = 1 Gbps

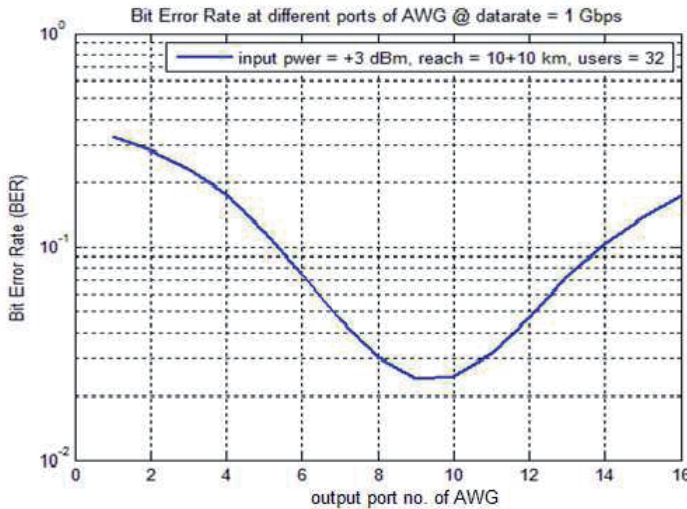


Fig. 6.7. Bit Error Rates on all 16 channels for input power = +3 dBm, reach = 10+10 Km & 32 users at a datarate = 1 Gbps

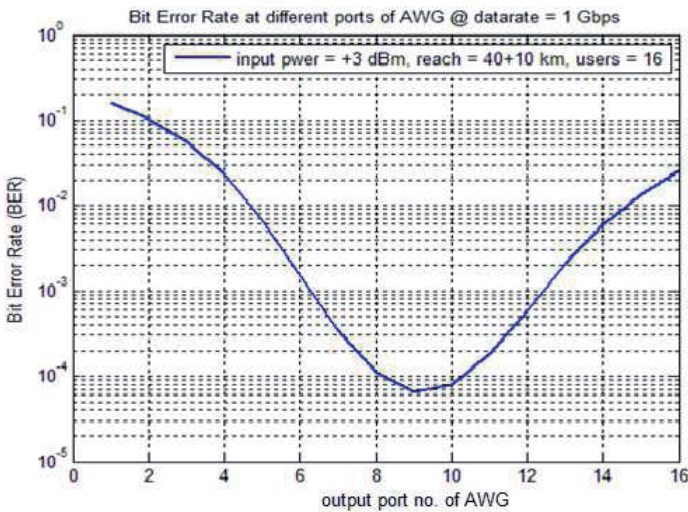


Fig. 6.8. Bit Error Rates on all 16 channels for input power = +3 dBm, reach = 40+10 Km & 16 users at a datarate = 1 Gbps

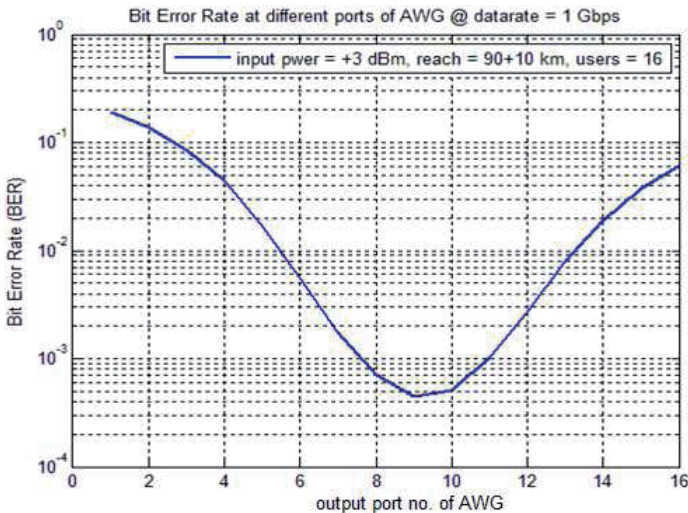


Fig. 6.9. Bit Error Rates on all 16 channels for input power = +3 dBm, reach = 90+10 Km & 16 users at a datarate = 1 Gbps

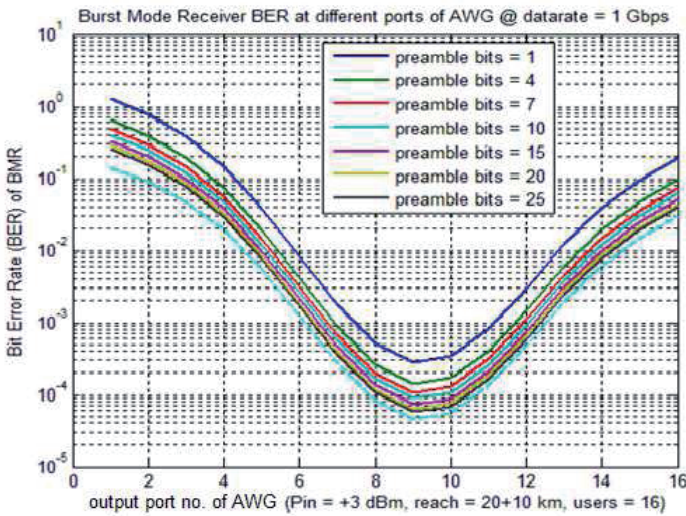


Fig. 6.10. Bit Error Rates on all 16 channels for input power = +3 dBm, reach = 20+10 Km & 16 users at a datarate = 1 Gbps with Burst Mode Receiver

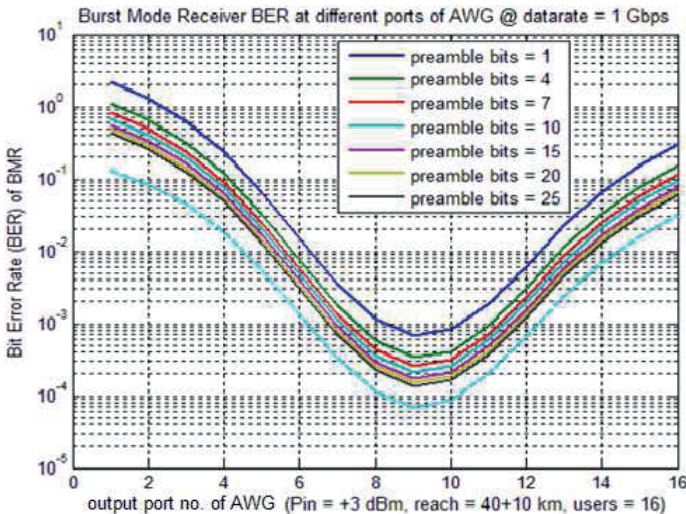


Fig. 6.11. Bit Error Rates on all 16 channels for input power = +3 dBm, reach = 40+10 Km & 16 users at a datarate = 1 Gbps with Burst Mode Receiver

Now, from Fig. 6.12 to Fig. 6.15, at first we see the BER at different channels for different reach distances for the architecture with CW laser near RN, when power

transmitted is +3 dBm in all channels, with a conventional receiver. In Fig. 6.16 and Fig. 6.17, we see the BER in all channels with BMR for different number of preamble bits. Clearly as reach distance increases, even with using more number of preamble bits, it becomes difficult to match the performance of a conventional receiver for a BMR. The cyan dashed blue line in these plots indicates the BER with a conventional receiver for the same reach distance.

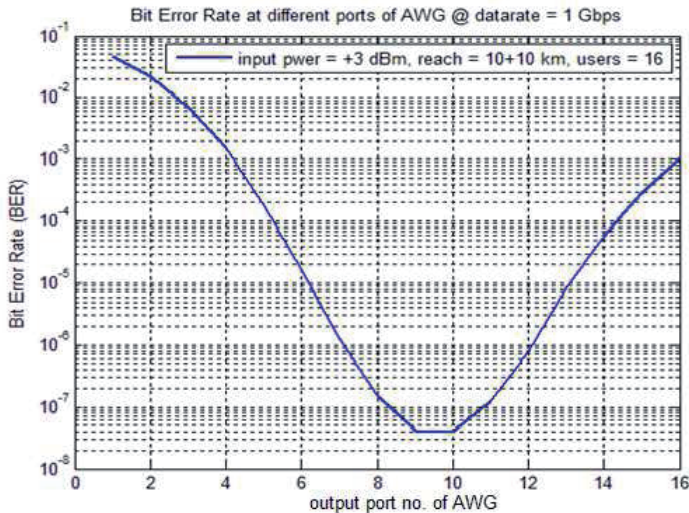


Fig. 6.12. Bit Error Rates on all 16 channels for input power = +3 dBm, reach = 10+10 Km & 16 users at a datarate = 1 Gbps

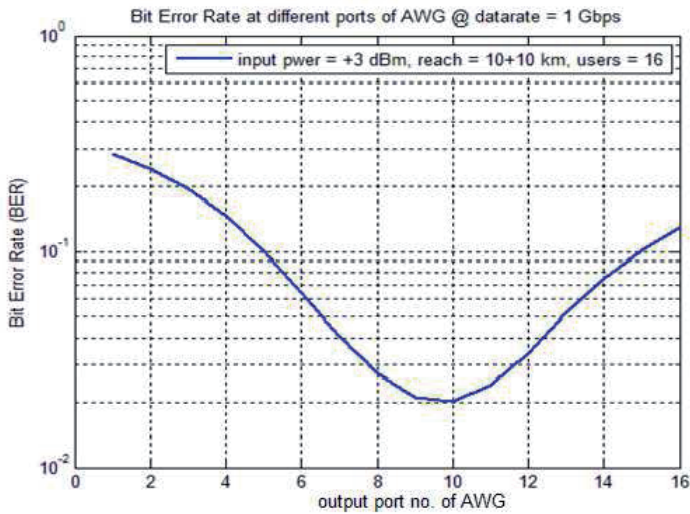


Fig. 6.13. Bit Error Rates on all 16 channels for input power = +3 dBm, reach = 10+10 Km & 32 users at a datarate = 1 Gbps

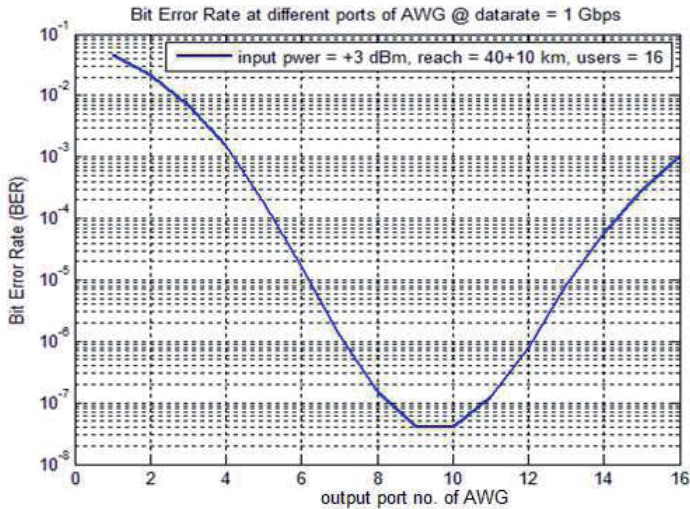


Fig. 6.14. Bit Error Rates on all 16 channels for input power = +3 dBm, reach = 40+10 Km & 16 users at a datarate = 1 Gbps

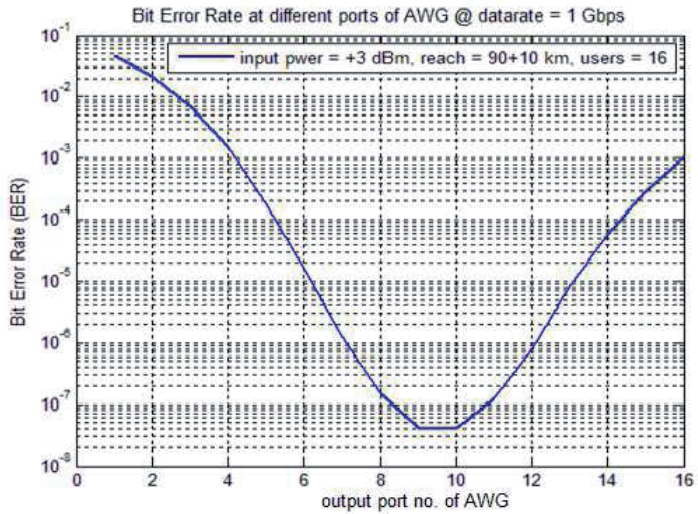


Fig. 6.15. Bit Error Rates on all 16 channels for input power = +3 dBm, reach = 90+10 Km & 16 users at a datarate = 1 Gbps

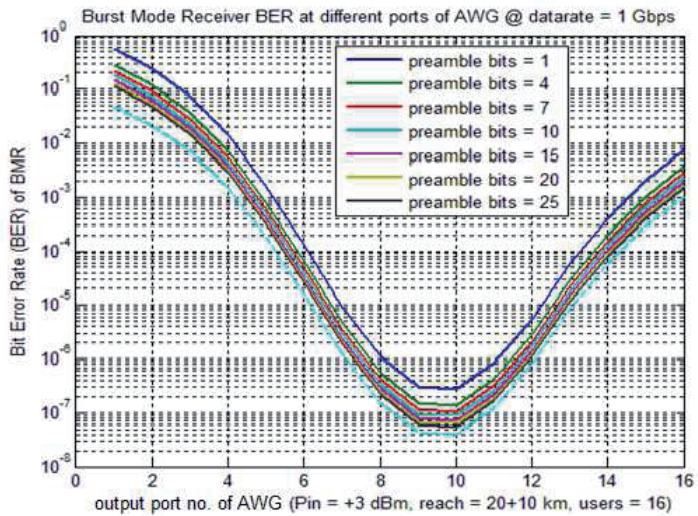


Fig. 6.16. Bit Error Rates on all 16 channels for input power = +3 dBm, reach = 20+10 Km & 16 users at a datarate = 1 Gbps with Burst Mode Receiver

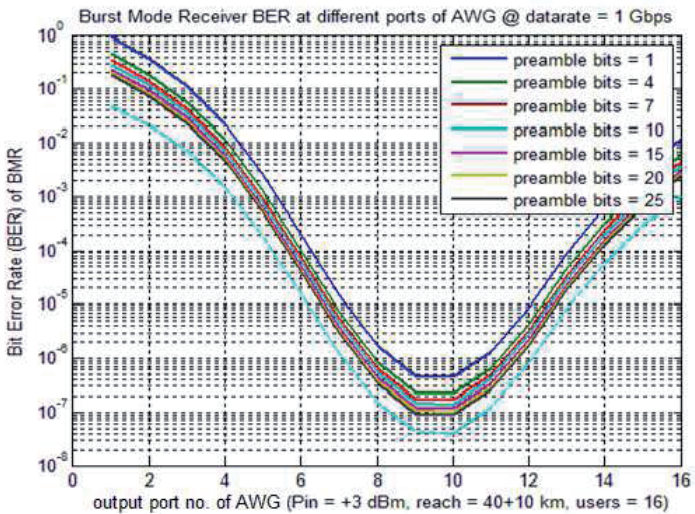


Fig. 6.17. Bit Error Rates on all 16 channels for input power = +3 dBm, reach = 40+10 Km & 16 users at a datarate = 1 Gbps with Burst Mode Receiver

Chapter 7

Conclusion and Future Work

7.1 Conclusion

In the end-to-end bit error rate analysis, the input signal powers in all the channels are considered +3 dBm. The crosstalk in AWG and amplifiers has been ignored for the sake of simplicity of the analysis. The RSOA based Long-Reach Passive Optical

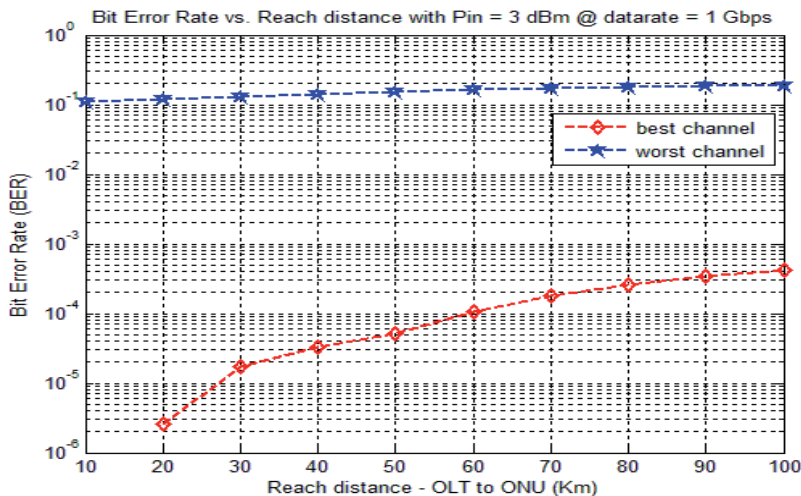


Fig. 7.1. Bit Error Rates of Best & Worst channels vs. reach of the RSOA based Long-Reach Passive Optical Network for architecture with CW lasers at OLT with input power = +3 dBm & 16 users at a datarate = 1 Gbps

Network is a noise based network and in this work the entire noise analysis of this type of network has been incorporated. The signals from CW lasers at OLT are noise free. As they pass through first EDFA, the attenuated signal is not only amplified, but also ASE noise is accumulated with them. After the intermediate stages, when the signals reach to RSOA, then a strong ASE signal is accumulated. Again, while returning back to OLT from ONU, signals are amplified as well as ASE accumulated by second EDFA.

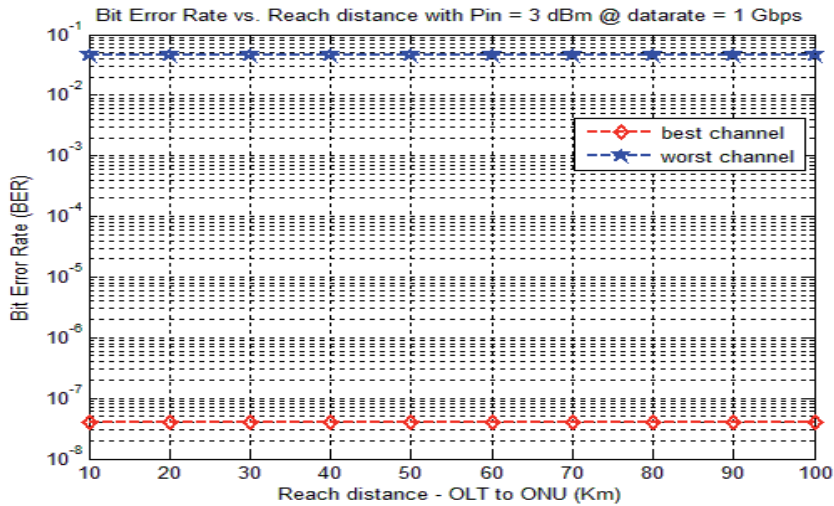


Fig. 7.2. Bit Error Rates of Best & Worst channels vs. reach of the RSOA based Long-Reach Passive Optical Network for architecture with CW lasers near RN with input power = +3 dBm & 16 users at a datarate = 1 Gbps

Thus finally depending on the signal and ASE powers arriving to the photodetector receivers at OLT, the BER with conventional receiver can be evaluated. Fig. 7.1 shows approximately the variation of best and worst channel BERs with distance, for the proposed architecture with CW lasers at OLT, as seen in Fig. 2.2. By following a similar method, the approximately the variation of best and worst channel BERs with distance, for the proposed architecture with CW lasers near RN, as seen in Fig. 2.3, is demonstrated in Fig. 7.2, which seems to be better than in Fig. 7.1 and variation with distance is also very negligible. Although, in both these architectures, the BER with conventional receiver is just around 10^{-8} in the best possible cases, which is much lower than conventional LR-PON architectures, which is lesser than 10^{-9} . Still, another 3 dB gain for the signal power is achievable by using advanced error control and equalization techniques [40][41]. Although, our findings of BER performance through analytical model goes well with the BER evaluated with the small scale experimental setup demonstrated in [41].

From the Fig. 7.1 and 7.2, it can be easily observed that the BER performance of architecture with CW lasers near RN is relatively better than architecture with CW lasers at OLT. From Fig. 3.8 and Fig. 3.10 in Chapter – 3, one can easily observe that if the signal power level goes below -15 dBm before falling upon RSOA, the ASE introduced in the network is huge and corrupts the signals almost completely. Thus, while designing any RSOA based network, one should carefully handle this aspect.

7.2 Scope of Future Work

7.2.1 End-to-end BER performance analysis in RSOA based hybrid TDM-WDM LR-PONs with Broadband Source (e.g., LED)

All the BER analysis done in this work is with the assumption that the CW optical sources are highly coherent lasers, with very sharp spectral density. But, maintenance of lasers is always a costly affair. So, instead of using the laser, a cheaper and no maintenance source like LED can be thought of as a replacement. The broader spectrum of LED will be divided into several channels automatically as it passes through AWG, as seen in Fig.4.1. But, then, all the models for EDFA, AWG & RSOA has to be re-done with Gaussian source profile, as frequency response of each AWG channel is Gaussian [22]. Although, intuitively, it can be expected the BER in this case will be little poorer than lasers.

7.2.2 Scheduling and Resource Allocation in RSOA based hybrid TDM-WDM LR-PONs

Along with the physical layer design issue, another trivial point of concern remains is the proper utilization of network resources. This can be ensured by designing proper access protocols in the media access (MAC) layer for this RSOA based hybrid TDM-WDM LR-PONs. While designing MAC protocols, the objective should be to maximize throughput as much as possible like the conventional hybrid TDM-WDM LR-PONs.

Appendix

A. Single pass gain in SOA & Double pass gain in RSOA

Let us consider a typical semiconductor optical amplifier (SOA) as shown in Fig. A.1 below. In this device, the light enters from the front facet, and then travels through the active region just like a waveguide and during this period it gets amplified, and then comes out of the rear facet.

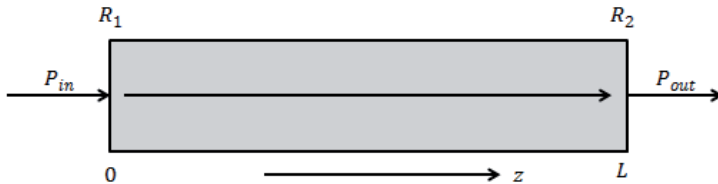


Fig. A.1. Light amplification in SOA

If we consider, the total length of the active region of an SOA is L , along the z -axis, then for every small length segment dz , the optical power is amplified by an amount $dP(z)$. If Γ is optical confinement factor, g_m is material gain coefficient and α is material loss coefficient, then for an input power P_{in} and output power P_{out} , the expression for single pass gain G_s [13], can be derived as follows:

$$dP(z) = (\Gamma g_m - \alpha) P(z) dz \quad (\text{A.1})$$

Integrating it over suitable limits, we get,

$$\int_{P_{in}}^{P_{out}} \frac{dP(z)}{P(z)} = \int_0^L (\Gamma g_m - \alpha) dz \quad (\text{A.2})$$

$$\text{or, } P_{out} = P_{in} \exp\{(\Gamma g_m - \alpha)L\} \quad (\text{A.3})$$

$$\text{or, } G_s = \frac{P_{out}}{P_{in}} = \exp\{(\Gamma g_m - \alpha)L\} \quad (\text{A.4})$$

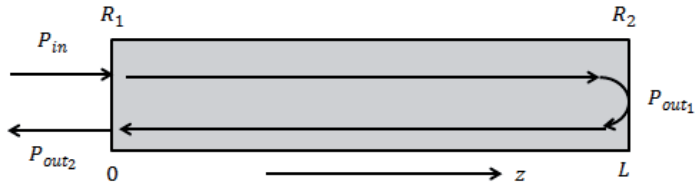


Fig. A.2. Light amplification in RSOA

Now, for RSOA, the light enters from the front facet, then travels through the active region just like a waveguide, gets reflected at the rear facet and again travels through the active region and during this period it gets amplified, and then comes out of the front facet again, as shown in Fig. A.2. So, for a similar device like above, the expression for double pass gain G_d can be derived, as follows:

$$P_{out_1} = P_{in} \exp\{(\Gamma g_m - \alpha)L\} \quad (\text{A.5})$$

and

$$P_{out_2} = R_2 P_{out_1} \exp\{(\Gamma g_m - \alpha)L\} \quad (\text{A.6})$$

$$\text{or, } P_{out_2} = R_2 P_{in} \exp\{2(\Gamma g_m - \alpha)L\} \quad (\text{A.7})$$

$$\text{or, } G_d = \frac{P_{out_2}}{P_{in}} = R_2 \exp\{2(\Gamma g_m - \alpha)L\} \quad (\text{A.8})$$

Thus, in general, if we have, $g = \Gamma g_m - \alpha$, then

$$(i) \quad \text{Single Pass Gain:} \quad G_s = \exp(gL) \quad (\text{A.9})$$

$$(ii) \quad \text{Double Pass Gain:} \quad G_d = R_2 \exp(2gL) \quad (\text{A.10})$$

Bibliography

- [1] L. G. Kazovsky, S.-W. Wong, V. Gudla, P. T. Afshar, S.-H. Yen, S. Yamashita and Y. Yan, "Challenges in next-generation optical access networks: addressing reach extension and security weaknesses," *IET Optoelectron. J.*, vol. 5, no. 4, pp. 133–143, Aug. 2011.
- [2] H. Song, B.-W. Kim, and B. Mukherjee, "Long-reach optical access networks: A survey of research challenges, demonstrations, and bandwidth assignment mechanisms," *IEEE Commun. Surv. Tutorials*, vol. 12, no. 1, pp. 112–123, 2010.
- [3] B. A. Forouzan, "Using Telephone and Cable Networks for Data Transmission," in *Data Communications and Networking*, 4th ed., New York: McGraw-Hill, 2006, pp. 241–261.
- [4] D. P. Shea, J. E. Mitchell, "Long-Reach Optical Access Technologies," *IEEE Network*, vol. 21, no. 5, pp. 5-11, Sep. 2007.
- [5] A. Banerjee, Y. Park, F. Clarke, H. Song, S. Yang, G. Kramer, K. Kim, and B. Mukherjee, "Wavelength-division-multiplexed passive optical network (WDM-PON) technologies for broadband access: a review," *J. Opt. Netw.*, vol. 4, no. 11, pp. 737–758, Nov. 2005.
- [6] J. Campany, D. Novak, "Microwave photonics combines two worlds," *Nature Photonics*, vol. 1, pp. 319–330, June 2007.
- [7] M. Ruffini, D. Mehta, B. O'Sullivan, L. Quesada, L. Doyle, and D. B. Payne, "Deployment Strategies for Protected Long-Reach PON," *IEEE/OSA J. Opt. Commun. Netw.*, vol. 4, no. 2, pp. 118-129, Feb. 2012.
- [8] D. B. Payne, R. P. Davey, "The Future of Fiber Access Systems?," *British Telecom Technol. J.*, vol. 20, no. 4, pp. 104-114, Oct. 2002.
- [9] S. Taebi, S. S. Saini, "Theory and Practice of a Polarization Independent Reflective SOA for WDM-PON Applications," *Optical Fiber Commun. & Optoelectronic Expo. & Conf.*, Asia, 2008.
- [10] X. Yu, T. B. Gibbon, I. T. Monroy, "Compact Wireless Access Nodes for WDM Bidirectional Radio-over-Fiber System Based on RSOA," *Conf. on Opt. Fiber Comm.*, San Diego, CA, 2009.
- [11] P. Chanciou, F. Payoux, T. Soret, N. Genay, R. Brenot, F. Blache, M. Goix, J. Landreau, O. Legouezigou and F. Mallécot, "Demonstration of RSOA-based remote modulation at 2.5 and 5 Gbit/s for WDM PON," *Conf. on Optical Fiber Commun. and the National Fiber Opt. Engineers Conf.*, Anaheim, CA, 2007.

- [12] M. J. Connelly, "Wideband Semiconductor Optical Amplifier Steady-State Numerical model," *IEEE J. Quantum Electron.*, vol. 37, no. 3, pp. 439-447, Mar. 2001.
- [13] M. J. Connelly, *Semiconductor Optical Amplifiers*, Kluwer Academic Publishers, 2002.
- [14] J. M. Senior, *Optical Fiber Communications*, 3rd Edition, Pearson, 2009.
- [15] A. Yariv, *Optical Electronics*, New York, HWR International, 1985.
- [16] N. G. Nilsson, "Empirical approximations for the Fermi energy of a semiconductor with parabolic bands," *Appl. Phys. Lett.*, vol. 33, pp. 653–654, 1978.
- [17] W. Shi, Z. Duan, R. Vafaei, N. Rouger, B. Faraji, L. Chrostowski, "Simulation of a 1550 nm InGaAsP-InP transistor laser," *Photonics and Optoelectronics Meetings (POEM) 2009: Optoelectronic Devices and Integration*.
- [18] J. Piprek, P. Abraham, and J. E. Bowers, "Self-consistent analysis of high-temperature effects on InGaAsP/InP lasers," *IEEE International Symposium on Compound Semiconductors, Berlin 1999*.
- [19] M. Liu, M. Zhang, L. Liu, Y. Zhan, Z. Liu, and P. Ye, "Numerical Modeling and Experimental Testing of Reflective Semiconductor Optical Amplifier (RSOA) with Modulation Bandwidth Optimization," in *Optical Transmission Systems, Switching, and Subsystems VIII*, Y. Su, E. Ciaramella, X. Liu, and N. Wada, eds., Vol. 7988 of Proceedings of SPIE-OSA (Optical Society of America, 2010)
- [20] Preliminary datasheet, SOA-RL-OEC-1550-TO 1.55 μm Reflective Semiconductor Optical Amplifier (SOA)
- [21] H. Takahashi, K. Oda, and H. Toba, "Impact of crosstalk in an arrayed-waveguide multiplexer on NxN optical interconnection," *J. Lightwave Tech.*, vol. 14, no. 6, Jun. 1996, pp. 1097–1105.
- [22] H. Takahashi, K. Oda, H. Toba, and Y. Inoue "Transmission Characteristics of Arrayed Waveguide NxN Wavelength Multiplexer," *J. Lightwave Tech.*, vol. 13, no. 3, Mar. 1995, pp. 447–455.
- [23] J. Salz, "Modulation and Detection for Coherent Lightwave Communications," *IEEE Commun. Mag.*, Vol. 24, No. 6, Jun. 1986, pp. 38-49.
- [24] M. K. Smit and C. V. Dam, "PHASAR-based WDM-devices: principles, design and applications," *IEEE J. Sel. Top. Quantum Electron.* vol. 2, no. 2, Jun. 1996, pp. 237–250.

- [25] J. Ratnam, S. Chakrabarti, and D. Datta, "Impact of Transmission Impairments on Demultiplexed Channels in WDM PONs Employing AWG-Based Remote Nodes," *J. Opt. Commun. Netw.*, vol. 2, no. 10, Oct. 2010, pp. 848-858.
- [26] P. C. Becker, N. A. Olsson, and J. R. Simpson, *Erbium-Doped Fiber Amplifiers Fundamentals and Technology*, Academic Press, 1997.
- [27] Y. Sun, A. K. Srivastava, J. Zhou, and J. W. Sulhoff, "Optical Fiber Amplifiers for WDM Optical Networks," *Bell Labs Technol. J.*, Jan-Mar. 1999, pp. 187-206.
- [28] C. R. Giles and E. Desurvire, "Modeling Erbium-Doped Fiber Amplifiers," *J. Lightwave Technol.*, vol. 9, no. 2, Feb. 1991, pp. 271-283.
- [29] Y. Sun, J. L. Zyskind, and A. K. Srivastava, "Average Saturation Level, Modeling, and Physics of Erbium-Doped Fiber Amplifiers," *IEEE J. Selected Areas in Quantum Electron.*, vol. 3, no. 4, Aug. 1997, pp. 991-1007.
- [30] D. Baney, "Optical Power and Wavelength for Single-Source Simulation of EDFA WDM Gain: Theoretical Basis," *HP Communications and Optics Research Laboratory Report*, Feb. 1996, pp. 1-8.
- [31] C. Berkdemir and S. Özsoy, "An investigation of the temperature dependency of the relative population inversion and the gain in EDFA by the modified rate equations," *Opt. Commun.*, vol. 254, no. 4, Jan. 2005, pp. 248-255.
- [32] P. R. Morkel and R. I. Laming, "Theoretical modeling of erbium-doped fiber amplifiers with excited-state absorption," *Opt. Lett.*, vol. 14, no. 19, Oct. 1989, pp. 1062-1064.
- [33] R. Ramaswami, K. N. Sivarajan, and G. H. Sasaki, *Optical Networks A Practical Perspective*, 3rd ed., Elsevier, 2010.
- [34] G. Keiser, *Optical Fiber Communications*, 4th ed., McGraw-Hill, 2000.
- [35] Preliminary datasheet, Calmer Optocom EDFA Datasheet for AMP-ST, AMP-LD & AMP-PM series EDFA, Rev. 110202.
- [36] C. A. Eldering, "Theoretical Determination of Sensitivity Penalty for Burst Mode Fiber Optic Receivers," *J. Lightwave Technol.*, vol. 11, no. 12, Dec. 1993, pp. 2145-2149.
- [37] C. Su, L.-K. Chen, and K.-W. Cheung, "Theory of Burst-Mode Receiver and Its Applications in Optical Multiaccess Networks," *J. Lightwave Technol.*, vol. 15, no. 4, Apr. 1997, pp. 590-606.

- [38] Y. Ota and R. G. Swartz, "Burst-Mode Compatible Optical Receiver With A Large Dynamic Range," *J. Lightwave Technol.*, vol. 8, no. 12, Dec. 1990, pp. 1897-1903.
- [39] Y. Ota, R. G. Swartz, and V. D. Archer, III, "DC-1Gb/s Burst-Mode Compatible Receiver for Optical Bus Applications," *J. Lightwave Technol.*, vol. 10, no. 2, Feb. 1992, pp. 244-249.
- [40] J.-H. Wu, J. Wu, and C.-N. Tsai, "Synchronous fibre-optic code division multiple access networks with error control coding," *Electronics Lett.*, vol. 28, no. 23, Nov. 1992, pp. 2118-2120.
- [41] Q. Guo and A. V. Tran, "Improving performance of MLSE in RSOA-based WDM-PON by partial response signaling," *Opt. Express*, vol. 19, no. 26, Dec. 2011, pp. 181-190.



yes I want morebooks!

Buy your books fast and straightforward online - at one of the world's fastest growing online book stores! Environmentally sound due to Print-on-Demand technologies.

Buy your books online at
www.get-morebooks.com

Kaufen Sie Ihre Bücher schnell und unkompliziert online – auf einer der am schnellsten wachsenden Buchhandelsplattformen weltweit! Dank Print-On-Demand umwelt- und ressourcenschonend produziert.

Bücher schneller online kaufen
www.morebooks.de

